Palaeogeography, Palaeoclimatology, Palaeoecology 617 (2023) 111493

Contents lists available at ScienceDirect

Palaeogeography, Palaeoclimatology, Palaeoecology

journal homepage: www.elsevier.com/locate/palaeo

Preservation of orbital forcing in intraplatform carbonates and an astronomical time frame for a multiproxy record of end-Triassic global change from a western Tethyan section (Csővár, Hungary)

Zsolt Vallner [a,b,*], Emma Blanka Kovács [c], János Haas [a], Ferenc Móricz [d], Micha Ruhl [c], Norbert Zajzon [d], József Pálfy [a,e]

[a] Department of Geology, Institute of Geography and Earth Sciences, Eötvös Loránd University, Pázmány Péter sétány 1/C, Budapest H-1117, Hungary
[b] Isotope Climatology and Environmental Research Centre (ICER), Institute for Nuclear Research, Bem square 18/C, Debrecen H-4026, Hungary
[c] Department of Geology, and Earth Surface Research Laboratory (ESRL), Trinity College Dublin, The University of Dublin, College Green, Dublin 2, Ireland
[d] Institute of Mineralogy and Petrology, University of Miskolc, Miskolc-Egyetemváros H-3515, Hungary
[e] ELKH-MTM-ELTE Research Group for Paleontology, Hungary

ARTICLE INFO

Editor: Prof. S Shen

Keywords:
Triassic-Jurassic boundary
End-Triassic extinction
Milankovitch cycles
Astrochronology
Depositional model
Aquifer eustasy

ABSTRACT

High temporal resolution is of paramount importance in stratigraphic studies of major events in earth history such as the end-Triassic extinction (ETE). Although it ranks among the most severe Phanerozoic mass extinctions, the precise timing and duration of the cascade of environmental and biotic changes across the Triassic-Jurassic boundary (TJB) interval remains controversial. Here we present a cyclostratigraphic study of the Csővár section (Hungary), a continuous carbonate succession from an intraplatform basin that yielded significant geochemical and paleontological data from around the TJB. We analyzed ten elemental time series and stable isotope data series and detected cyclicities with periodicities similar to the orbital cycles of the ~405 kyr long and ~124 kyr short eccentricity, the ~34 kyr obliquity, and the ~17–21 kyr precession. The astrochronologic age model suggests that the ~52 m thick section was deposited in 2.9–3 Myr, with an average sedimentation rate of 1.73–1.79 cm/kyr. We establish that the section contains the last ~1.3 million years of the Rhaetian and most of the Hettangian, supporting a <2 Myr duration for this stage. The duration of the initial carbon isotope anomaly (ICIE) is estimated at ~40–80 kyr. Previously recognised meter-scale sequences are in agreement with the long eccentricity cycles up to the level of the ICIE but subsequently this relationship becomes less clear, possibly reflecting the effects of the end-Triassic climatic/environmental perturbations and associated changes in the depositional environment superimposed onto overarching astronomical forcing. We propose a cyclicity-based environmental model for sedimentation in the Csővár basin where the observed antiphase behaviour of the carbonate accumulation and the terrigenous input and dissolved silica was driven by a combination of aquifer- and limno-eustasy and the "megamonsoon" system that dominated the climate of the peri-Tethyan realm. This study highlights that intraplatform carbonate successions can be suitable archives to preserve orbital cyclicities and the new astrochronological age model helps improve our understanding of the ETE and other events in the TJB interval.

1. Introduction

The end-Triassic extinction (ETE) is one of the most severe Phanerozoic biotic crises (Sepkoski, 1996) that is related to major environmental changes associated with super greenhouse warming (McElwain et al., 1999) and ocean acidification (Greene et al., 2012), linked to perturbations in the carbon cycle (Pálfy et al., 2001; Ward et al., 2001; Hesselbo et al., 2002). Recognition of synchrony with volcanism in the Central Atlantic Magmatic Province (CAMP) (Marzoli et al., 1999) led to an emerging consensus that CAMP activity triggered a complex cascade

* Corresponding author at: Department of Geology, Institute of Geography and Earth Sciences, Eötvös Loránd University, Pázmány Péter sétány 1/C, Budapest H-1117, Hungary.
E-mail addresses: zsolt.vallner@gmail.com (Z. Vallner), kovacse@tcd.ie (E.B. Kovács), haas@staff.elte.hu (J. Haas), ferenc.moricz@uni-miskolc.hu (F. Móricz), Micha.Ruhl@tcd.ie (M. Ruhl), askzn@uni-miskolc.hu (N. Zajzon), palfy@elte.hu (J. Pálfy).

https://doi.org/10.1016/j.palaeo.2023.111493
Received 27 August 2022; Received in revised form 24 February 2023; Accepted 5 March 2023
Available online 11 March 2023

of environmental and biotic changes (Pálfy and Kocsis, 2014). However, nuanced understanding of the cause-and-effect relationships and modeling of various aspects of Earth system changes require an accurate temporal framework that has remained controversial across the Triassic-Jurassic transition.

A timeframe using zircon U-Pb ages was developed in volcanic ash-bearing marine successions of North and South America (Pálfy et al., 2000; Schaltegger et al., 2008; Guex et al., 2012) but problems remain in ammonite-based biostratigraphic correlation with European sections. Alternatively, cyclostratigraphic analyses were carried out leading to development of astrochronologies in marine sections in the UK (Weedon et al., 1999; Ruhl et al., 2010; Hüsing et al., 2014; Xu et al., 2017; Weedon et al., 2019; Storm et al., 2020), the GSSP in Austria at Kuhjoch (Galbrun et al., 2020) and deep marine cherts in Japan (Ikeda and Tada, 2014), as well as in terrestrial sections from Pangean rift basins in eastern North America (Olsen and Kent, 1996; Kent et al., 2017) and Morocco (Deenen et al., 2010), and the Junggar Basin in China (Sha et al., 2015). However, some of the marine successions are plagued with problems of hiatuses and/or major facies changes near the Triassic-Jurassic boundary (TJB). The terrestrial sections inherently present correlation issues with the marine realm that have not yet been unambiguously resolved by magnetostratigraphy or other independent methods including radiometric dating (Olsen and Kent, 1996; Blackburn et al., 2013; Kent et al., 2017). In addition, the fossil record of biotic change and geochemical proxy records of environmental change are often derived from other sections whose correlation is challenging (e.g. Jost et al., 2017; He et al., 2020). Nevertheless, these studies of successions deposited in remarkably different environments suggest that during the TJB interval, despite the severe effects of CAMP volcanism, many sedimentary systems preserved the signal of the orbitally forced cyclicity.

Here, we present the results of a cyclostratigraphic study of the Vár-hegy section at Csővár (Hungary) that straddles the TJB (Pálfy and Dosztály, 2000). This succession was deposited in an intraplatform basin and its carbonate sedimentology is well characterized (Haas and Tardy-Filácz, 2004), with previous sequence stratigraphic analysis suggesting the presence of decimeter- and meter-scale cycles (Haas et al., 2010). The section is one of the first localities worldwide where the initial carbon isotope excursion (ICIE) marking the end-Triassic carbon cycle perturbation associated with the end-Triassic mass extinction, was recognized (Pálfy et al., 2001), and it has a robust biostratigraphic framework based on ammonites, conodonts and radiolarians (Kozur and Mock, 1991; Pálfy et al., 2001, 2007; Karádi et al., 2019). Additional signatures of the end-Triassic events include synchronous peaks of spores and prasinophytes (Götz et al., 2009) and the largest peak of sedimentary mercury concentrations reported so far from the TJB interval (Kovács et al., 2020). The uniform lithology, the absence of major facies changes throughout, including the TJB interval, and the lack of conspicuous hiatuses (Haas and Tardy-Filácz, 2004; Pálfy et al., 2007) make this section potentially well-suited for a cyclostratigraphic and astrochronologic study.

The aim of this study is to develop an astrochronological age model to provide a high-resolution temporal framework for this time-interval, and to facilitate correlation with other sections characterized by records of global environmental change. We applied multiproxy cyclostratigraphy that also allowed us to assess the environmental drivers of the preserved cyclicity (Li et al., 2019a; Sinnesael et al., 2019). We have detected dominant Milankovitch cycles and established the astronomical duration of the section, refined the placement of the Triassic-Jurassic boundary here, and assessed the duration of the Initial Carbon Isotope Excursion (ICIE). Our results bear on the timing and sequence of biotic and geochemical events across this pivotal interval of Earth history. In addition, we attempted to interpret the cyclic environmental variations in the Csővár basin and associated cyclic sedimentation in this intraplatform carbonate system in a novel way, invoking the influence of a "megamonsoon" climate regime as the driver of eustasy at the TJB.

2. Geological and stratigraphic background

2.1. Geological setting

The village of Csővár is located about 40 km north-northeast of Budapest in north-central Hungary. Exposures of the Triassic-Jurassic boundary (TJB), the Pokol-völgy quarry and the section on the south slope of the Vár-hegy ('Castle Hill') lie west-northwest of the village (Fig. 1). Stratigraphic studies of the surface outcrops are complemented by the 1200 m deep Csv-1 well drilled in 1968 in the lower yard of the Pokol-völgy quarry (Haas et al., 1997).

The fault-bounded, uplifted Nézsa-Csővár block on the left side of the Danube comprises the northeasternmost surface exposures of the Transdanubian Range (TDR) tectonic unit that forms part of the Alcapa mega-unit (Haas and Tardy-Filácz, 2004), a composite terrane within the Alpine-Carpathian orogenic system. Overlain, following a major unconformity, by Eocene and Oligocene strata, the Upper Triassic to Lower Jurassic marine carbonates are assigned to the Csővár Formation. This unit is composed of slope, toe-of-slope and basinal sediments deposited in one of the intraplatform basins developed in the outer part of the Dachstein platform system, on the western shelf of the Neotethys (Fig. 2) (Haas and Tardy-Filácz, 2004; Haas et al., 2010).

The Csv-1 well penetrated an Upper Carnian to Lower Rhaetian succession (Karádi et al., 2013). Most of the strata exposed in the Pokol-völgy quarry are Rhaetian in age based on ammonites and conodonts, whereas the partially overlapping Vár-hegy section on the opposite side of the valley extends from the Upper Rhaetian to Sinemurian, on the basis of observed conodonts, radiolarians and ammonites, and thus contains the Triassic-Jurassic boundary (Kozur, 1993; Haas et al., 1997; Pálfy and Dosztály, 2000; Haas and Tardy-Filácz, 2004; Haas et al., 2010). Both measured stratigraphic sections in the Pokol-völgy quarry and on the Vár-hegy are assigned to the Csővár Formation (Haas et al., 1997; Haas and Tardy-Filácz, 2004; Pálfy and Haas, 2012).

Development of the Csővár basin started in the early Carnian when

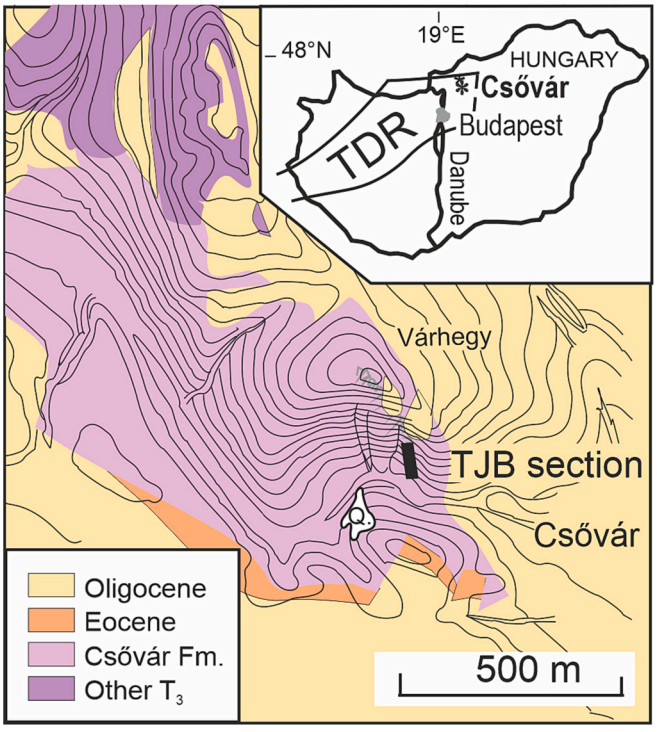

Fig. 1. Location of the Csővár section and simplified geology of the south-eastern part of the Csővár block. Abbreviations: TDR – Transdanubian Range, Q. – Pokol-völgy quarry, Fm. – Formation, T_3 – Upper Triassic (after Benkő and Fodor, 2002, Pálfy et al., 2001 and Pálfy et al., 2007).

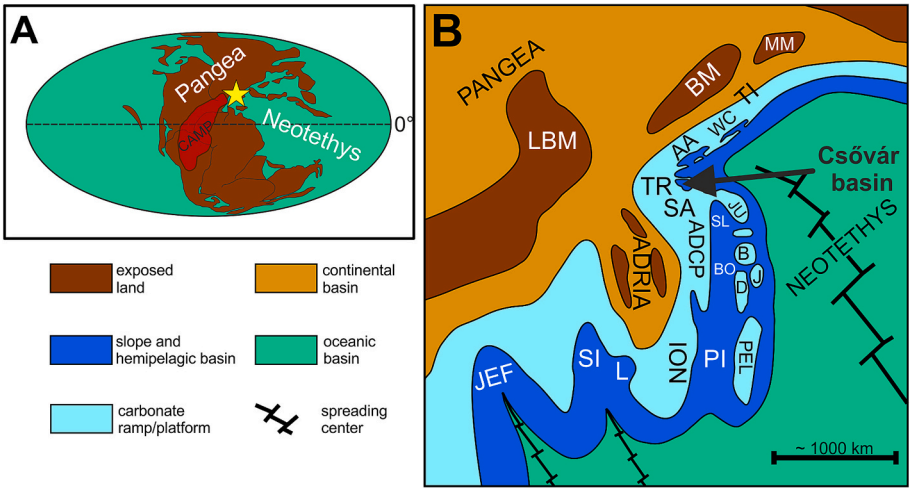

Fig. 2. Location of the Csővár basin at the Triassic-Jurassic transition, (A) in a global paleogeographic context and (B) in the regional reconstruction of the westernmost Neotethys (Haas et al., 2019). CAMP: Central Atlantic Magmatic Province, LBM: London-Brabant Massif, BM: Bohemian Massif, MM: Malopolska Massif, AA: Austroalpine Units, WC: Central and Inner West Carpathian Units, TI: Tisza Unit, TR: Transdanubian Range, SL: Slovenian basin, JU: Julian Alps, B: Bukk Unit, ADCP: Adriatic-Dinaridic Carbonate Platform, BO: Bosnian Zone, D: Drina–Ivanjica Unit, J: Jadar Block, SI: Sicilian Basin, L: Lagonegro Basin, JEF: Jefra Basin, PI: Pindos Basin, PEL: Pelagonian-Subpelagonian Units. Adapted from Kovács et al. (2020).

extension related to rifting in the westernmost Neotethys opened narrow intraplatform basins at the northeastern end of the Dachstein platform parallel to the platform margin. The Hármashatárhegy basin is another similar but more restricted and hence oxygen-depleted intraplatform basin nearby known from exposures and drill cores in Budapest. The Csővár and Hármashatárhegy basins either formed a single intraplatform basin with parts of different degrees of restriction, or, existed as individual basins separated by platforms and/or islands (Haas et al., 2000; Haas, 2002). Common terrestrial plant remains that occur throughout the succession at Csővár, their variable size, and the abundance of elongated phytoclasts, pollens and spores suggest that small islands existed on the outer platform during the Triassic-Jurassic transition interval (Haas et al., 2010).

Late Carnian to Norian basinal sedimentation was gradually replaced by a toe-of-slope depositional environment by the end of the Norian, indicating progradation of an adjacent carbonate platform (Haas and Budai, 1999; Haas, 2002; Benkő and Fodor, 2002). The lowermost Rhaetian basal part of the Pokol-völgy quarry section suggests a significant sea level drop wich may have resulted in subaerial exposure of the nearby platform, increase in terrestrial plant debris, and oxygen-depleted bottom waters in the basin (Haas and Budai, 1999; Haas and Tardy-Filácz, 2004). The Lower Rhaetian layers contain proximal calcareous turbidite layers with crinoid fragments. Common terrestrial palynomorphs indicate that much of the adjacent platforms remained emerged. The onset of transgression led to the establishment of small buildups on the highest parts of the slope. Debris flow deposits and synsedimentary slump structures became common, suggesting sediment movement along the slope (Haas and Tardy-Filácz, 2004; Haas et al., 2018). As recorded in the topmost part of the quarry and the lower part of the Vár-hegy section, continuing relative sea level rise in the Early Jurassic controlled a gradual upward shift from predominantly proximal to distal calcareous turbidites and then finally to the basinal deposits. At 32 m above the base of the Vár-hegy section, lower Hettangian beds with redeposited oncoids and grapestones occur which may have derived from ambient submarine highs (Haas and Tardy-Filácz, 2004). Above the measured section, near the top of Vár-hegy cherty limestone becomes predominant and extends into the Sinemurian stage (Kozur, 1993).

2.2. Biostratigraphic framework

Although most fossil groups occur rather sparsely, the local record of ammonoids, conodonts, radiolarians, foraminifera and palynomorphs are adequate to construct a well-resolved biostratigraphic framework and constrain the placement of the Triassic-Jurassic boundary to a narrow stratigraphic interval. The primary marker for the definition of the Triassic-Jurassic boundary and the key fossils for high-resolution Jurassic biostratigraphy are ammonoids (Hillebrandt et al., 2013), but in the Vár-hegy section only a few poorly or moderately preserved specimens have been found. The lowermost 10 m of the section (up to Bed 27) yielded ammonites of Rhaetian age (*Choristoceras* spp., *Cladiscites* sp.), which suggests that this part belongs to the upper Triassic Marshi Zone (Pálfy and Dosztály, 2000). The first unambiguously Jurassic ammonoid (*Psiloceras* sp.) was recovered at 29.5 m (Bed 66), although one specimen of *Nevadaphyllites psilomorphum* (also Jurassic in age) was found *ex situ* at 19 m (Pálfy and Dosztály, 2000; Pálfy et al., 2001). *Waehneroceras* sp. collected from the top of the section (~54 m) indicates a middle Hettangian age (Pálfy and Dosztály, 2000), whereas the most recent study reported the co-occurrence of *Schlotheimia* sp. and Juraphyllitidae gen. et sp. indet. from ~52 m, indicating the base of the upper Hettangian Marmorea Zone (Kovács et al., 2020).

Based on radiolarians, the uppermost Rhaetian *Globolaxtorum tozeri* zone is identified at ~1.5 m (Bed 4), whereas the lower Hettangian *Relanus hettangicus* zone is identified at ~26.5 m (Bed 62) (Pálfy et al., 2007).

Previously, the lowermost beds of the section were assigned to the *Misikella posthernsteini* conodont zone (Kozur and Mock, 1991; Pálfy et al., 2007), but recent studies suggest that the entire lower 10.5 m of the succession (up to Bed 29) can be assigned to the *Misikella ultima* zone (Karádi et al., 2019). Single specimens of both *Misikella ultima* and *'Neohindeodella'* sp. were found at 20.9 m (Bed 54) but their reworking cannot be ruled out (Pálfy et al., 2007). The highest conodont occurrence, *Neohindeodella detrei* was found at 31.7 m (Bed 74) and is considered to be a sole survivor of the end-Triassic extinction (Kozur, 1993; Pálfy et al., 2007; Du et al., 2020).

The lowermost 12.5 m of the section is characterised by a rich and diverse fauna of Rhaetian foraminifera but only an impoverished assemblage occurs above this level. The last specimens of certain Triassic age were found at 14.5 m (Bed 36), whereas the first definitive Jurassic species (*Involutina liassica*) appears at 52 m (Bed 119) (Pálfy et al., 2007).

Palynomorphs of Rhaetian age are present up to ~20 m (Bed 49). A sudden increase in the abundance of prasinophytes (*Tasmanites*), and a concomittant peak abundance of trilete spores (*Concavisporites* spp., *Deltoidospora* spp.) is recorded at ~19 m (Bed 47) (Götz et al., 2009).

Thus, if the contentious find of *Misikella ultima* in Bed 54 (20.9 m) is not considered, the palynomorphs from Bed 49 (~20 m) represent the highest occurrence of Triassic fossils. On the other hand, the stratigraphically lowest Jurassic fossils, radiolarians, originate from Bed 62 (~26 m). Thereby the TJB is biostratigraphically constrained to a 6 m thick boundary interval between Beds 49 and 62 of the studied section.

3. Material and methods

3.1. Sampling and hand-held XRF measurements

We sampled 51.8 m of the measured stratigraphic section at Várhegy near Csővár that contains the Triassic-Jurassic boundary, and which has been the subject of detailed studies previously (Haas and Tardy-Filácz, 2004; Pálfy et al., 2007; Kovács et al., 2020). A total of 243 samples were collected with a uniform sample spacing of 20 cm except for three short intervals at 15.2–15.8 m, 17.8–18.4 m and 21.8–24.6 m (i.e. Beds 40, 45 and 59). There, the thickest slump beds were excluded from the sampling as they are considered to result from instantaneous sedimentation events that would adversely affect any cyclostratigraphic analysis (Weedon, 2003).

For comprehensive elemental analyses, the entire suite of 243 samples was processed and ground in a tungsten carbide mortar, as the use of tungsten carbide devices would exclude any contamination other than tungsten and cobalt (Yamasaki, 2018). Calcite veins and weathered surfaces were carefully removed from the rock fragments. Pulverization was performed by a tungsten carbide Fritsch pulverisette 02102 type pulverizer at the Department of Mineralogy of Eötvös Loránd University. The mortar and the pulverizer were thoroughly cleaned and dried after processing each sample.

XRF analyses were carried out using an Olympus Vanta C Series hand-held X-Ray Fluorescence Analyzer with rhodium anode at the University of Miskolc. During the measurement the factory-standard Geochem (2) mode was used with analysis times of 30 and 60 s. For the former the voltage was 40.01 kV and the amperage was 100.05 μA, whereas for the latter the voltage was 9.98 kV and the amperage was 200 μA. Based on experience, this measurement time is sufficient for all hand-held XRF instruments (Quye-Sawyer et al., 2015; Ruhl et al., 2016; De Winter et al., 2017; Sinnesael et al., 2018; Saker-Clark et al., 2019). 6–7 g of rock powder was weighed, placed on a paper holder (which was changed after every sample), and after leveling the surface, it was covered with 2.5 μm thick Chemplex Mylar polyester film. The Mylar film was cleaned after each sample and replaced after every tenth sample or immediately after any damage was noticed to the film. Mylar film was shown to have only a negligible effect on the measurements, which was systematic for all samples, and it does not affect cyclostratigraphic studies (Quye-Sawyer et al., 2015). The instrument aperture was held tightly into the powder through the film during the measurement, thus reducing the error due to the air content in the pore space of the powder.

Hand-held XRF instruments are less accurate than benchtop models as they have higher detection limits for most elements and their capability is limited to the measurement of fewer elements. However, there is ample evidence that the accuracy of the hand-held XRF instruments is adequate for cyclostratigraphic studies (Ruhl et al., 2016; Sinnesael et al., 2018; Saker-Clark et al., 2019) and they allow for efficient data collection for carbonate rocks (Quye-Sawyer et al., 2015; Ruhl et al., 2016; De Winter et al., 2017; Sinnesael et al., 2018).

3.2. Time series analysis

A total of 34 elemental datasets were generated in oxide form by XRF measurements, including: MgO, Al_2O_3, SiO_2, PO, SO, K_2O, CaO, TiO_2, VO, CrO, MnO, FeO, CoO, NiO, CuO, ZnO, AsO, SeO, Rb_2O, SrO, Y_2O_3, ZrO_2, NbO, MoO, AgO, CdO, SnO, SbO, WO, HgO, PbO, BiO, ThO_2 and UO. For five of them, SiO_2, PO, CaO, FeO and SrO, all samples yielded measurable values, i.e. above the detection limit (Table S1). The concentration of five additional elements fell below the limit of detection (LOD) in only a few samples, thus it was also possible to perform cyclostratigraphic analysis on these datasets: TiO_2 (44 samples <LOD), VO (68 samples <LOD), MnO (28 samples <LOD), ZnO (85 samples <LOD), and ZrO_2 (68 samples <LOD). In addition, the $\delta^{13}C_{carb}$ and $\delta^{18}O$ datasets with better than ±0.1‰ accuracy and reproducibility obtained by Kovács et al. (2020) from the same suite of samples were also suitable and utilized for time series analysis.

Thus, a total of 12 time series (see Fig. 3 for the best quality datasets) from the Csővár section were available for analysis (Table S1), with each of them interpreted as a uniformly spaced, continuous-signal record. Details of the procedure for processing each time series for the analysis are provided in the Supplementary material, except for the time series of PO, SrO, ZnO, and ZrO_2, that did not show any significant astronomical signal after experimenting with every possible settings and data preparation options.

Time series analysis was performed using the *Acycle* software (v. 2.2) (Li et al., 2019a). Power spectra were generated using zero-padding (Bloomfield, 1976) and the Multi-taper Method (Thomson, 1982; Mann and Lees, 1996). The confidence levels on power spectra were generated using a robust autoregressive (robust AR (1) model (Mann and Lees, 1996)). The evolutionary spectra were generated using 1500 cm wide sliding windows and 20 cm steps (Kodama and Hinnov, 2015). To test the hypothesis that observed cycles matched with Milankovitch frequencies for that time-interval, we used the frequency ratio method which compares the frequency ratios of the identified cycles and the Milankovitch cycles. Subsequently observed dominant periodicities were also compared to results of the more sophisticated COCO and eCOCO methods in the *Acycle* software (Li et al., 2018b; Li et al., 2019a). These methods simultaneously test the best match between the studied power spectra and the power spectra of the La2004 astronomical solution (Laskar et al., 2004) for the studied time interval to determine the most likely sedimentation rate and the number of Milankovitch cycles present in the signal. These methods were applied to the SiO_2 and CaO time series (for details see chapter S3 in the Supplementary material). A Gaussian bandpass filter (Kodama and Hinnov, 2015) was used for filtering the 0.00133 ± 0.00027 cycles/cm frequency in each time series. Assuming that this frequency corresponds to the long excentricity cycle, an age model was created in which the age difference of successive maxima (and minima) of the filtered signal represents 405 kyr. In addition, wavelet analysis was performed on the SiO_2 and CaO time series (Torrence and Compo, 1998).

4. Results

4.1. Elemental geochemistry

There are no significant trends or conspicuous anomalies in the elemental data series, which reflects the remarkably homogenous lithology of the Csővár Formation. The main characteristics of the six successfully analyzed elemental data series (Fig. 3) are as follows: the minimum of the SiO_2 content is 0.36 wt% (at 4.8 m), whereas its maximum is 14.5 wt% (at 19.4 m), the average of the SiO_2 content is 2.56 wt%. The minimum of the CaO content is 20.66 wt% (at 50.2 m), whereas its maximum is 40.32 wt% (at 0 m), the average is 35.47 wt%. The minimum of the TiO_2 content (where >LOD) is 0.025 wt% (at 10.8 m), whereas the maximum is 0.28 wt% (at 28.6 m), the average (without <LOD) is 0.082 wt%. The minimum of the VO content (where >LOD) is 0.004 wt% (at 6.4 m), whereas the maximum is 0.025 wt% (at 1.4 m), the average (without <LOD) is 0.0098 wt%. The minimum of the MnO content (where >LOD) is 0.0043 wt% (at 32.2 m), whereas the maximum is 0.048 wt% (at 30 m), the average (without <LOD) is 0.016 wt%. The minimum of the FeO content is 0.016 wt% (at 5.2 m), whereas the maximum is 1.27 wt% (at 13.2 m), the average is 0.17 wt%.

4.2. Cyclostratigraphy

Three prominent periodicities were detected in the Csővár section, which are present in the signal of almost every time series. The amplitude of these cycles greatly exceeds the of analytical error (for more detail see the Supplementary material). The range and mean value (in parentheses) of their frequencies are as follows: 0.0011–0.00165

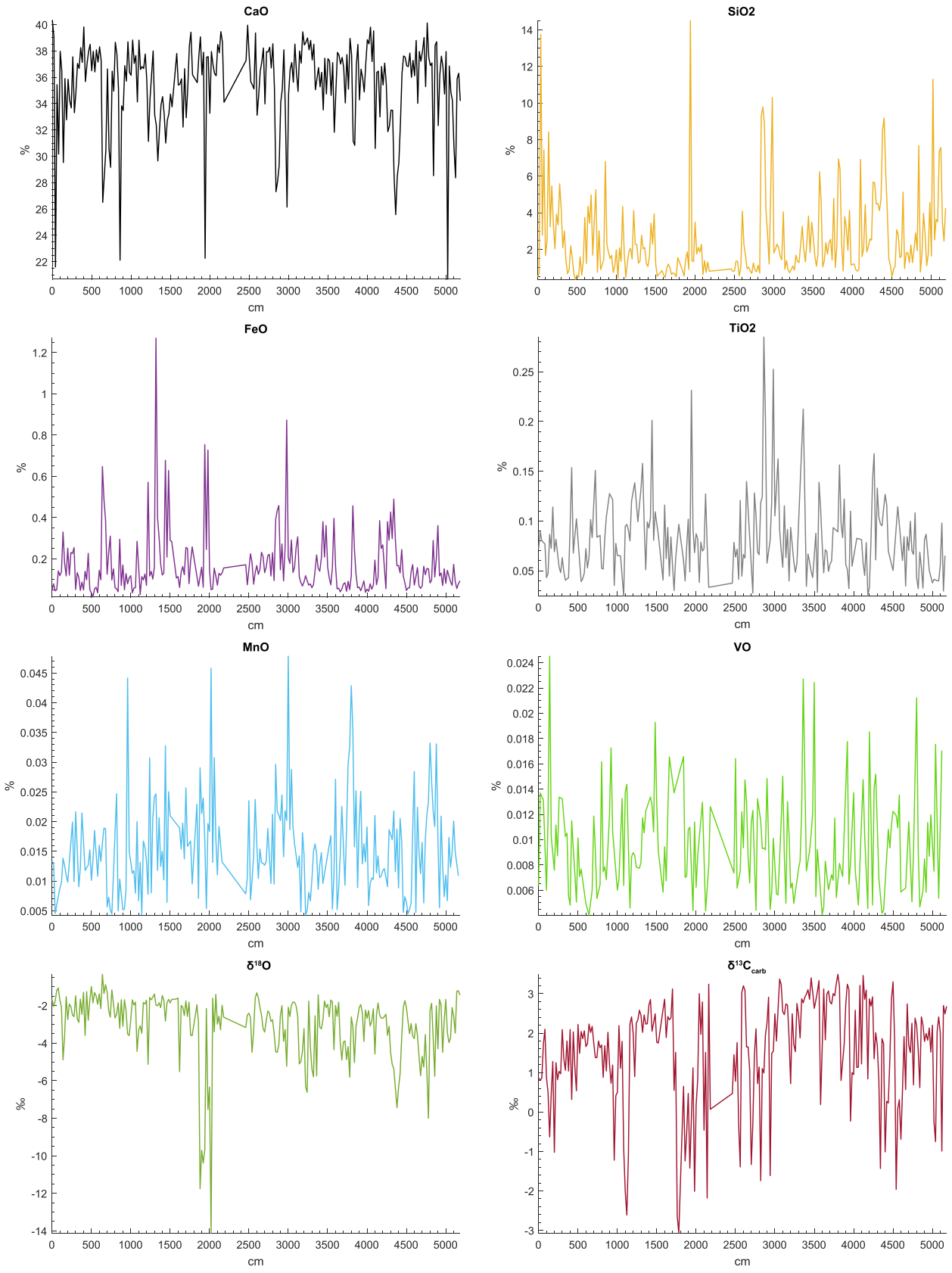

Fig. 3. Raw time series of the best quality elemental and stable isotope data series from the Csővár, Vár-hegy section. Stratigraphic position above the base of the measured section shown in the horizontal axis; percentage values in oxide form for the elemental data series, and permil values for the stable isotope data series are shown in the vertical axis.

(0.00133), 0.0033–0.0055 (0.00415), and 0.013–0.016 (0.015) cycles/cm (Fig. 4). The validity of these periodicities and their frequencies was confirmed by F-tests. The evolutionary spectra demonstrated that each could be detected throughout most of the section, with the exception of the frequency of 0.015 cycles/cm that is not traceable in the lower c. 25 m of the succession (Fig. 5). Cutting the time series into two equal, not overlapping parts, and analysing them separately also results in the recognition of the same three periodicities in both parts of the succession in almost every analyzed time series, confirming their likely validity to represent actual cycles. The generated power spectra and evolutionary spectra reveal that the cycles change their frequencies but maintain their relative period ratios at c. 25 m. From 0 to 25 m, cycle frequencies decrease gradually, whereas at c. 25 m they become stable and remain continuously expressed up to the top of the analyzed section at 51.8 m (Fig. 5). Probably for the same reason, the frequency of 0.015 cannot be observed below 25 m, because in order to maintain the period ratio compared to the lower frequencies, it has to produce too large sideways steps in terms of frequency and therefore its signal is weak and fragmented (Fig. 5).

At approx. 21–25 m, the evolutionary spectra of several proxy time series display a shift towards lower frequencies while maintaining their ratio. This phenomenon is likely an artifact caused by the lack of data in the interval between 21.8 and 24.6 m that is dominated by slumps.

Changes in the frequency for a given cycle throughout the section likely resulted from changes in the sedimentation rate. The continuous decrease of frequencies up to 25 m indicates a continuous increase of the sedimentation rate that peaks between 21 and 25 m. From here, both the frequencies of cycles and the sedimentation rate remain nearly constant.

Some proxy time series reveal additional periodicities with frequencies of 0.007–0.0088 and 0.021–0.023 cycles/cm. Although the results of the F-test would not exclude that these are real cycles, their signal in the evolutionary spectra (Fig. 5) suggests that these frequencies rather belong to the background noise. The periodicity with the frequency range of 0.007–0.0088 cycles/cm does not appear in about half of the time series, whereas in the power spectra and evolutionary spactra it is common that noise peaks appear near the highest detectable frequency, i.e. the Nyquist frequency (Weedon, 2003). Since the Nyquist frequency for the time series of Vár-hegy section is 0.025 cycles/cm, it may explain the emergence of strong background noise in the 0.021–0.023 cycles/cm frequency range.

The results of pairing the observed cycles with Milankovitch cycles using the frequency ratio method is presented in Table 1. The periods of the three dominant frequencies (0.00133, 0.00415, and 0.015 cycles/cm) are ~752, 241, and 67 cm. A comparison of their ratios with the those of the periodicities of dominant Milankovitch cycles at that time yields the best agreement by assigning the 752 cm cycle to the long eccentricity, the 241 cm cycle to the short eccentricity, and the 67 cm cycle to the obliquity cycle. It follows that if the period of the 752 cm cycle is 405 kyr, then the period of the 241 cm cycle is 129 kyr, and the period of the 67 cm cycle is 36 kyr. Comparing this with the periods of the corresponding Milankovitch cycles as calculated by the La2004 astronomical solution for the Triassic-Jurassic boundary (Table 1), there is reasonable agreement to one characteristic period of short eccentricity at 124 kyr and the dominant period of obliquity at 34 kyr (Laskar et al., 2004). If the periodicity of 0.007–0.0088 cycles/cm is considered as a real cycle, it would correspond to a period of 61–77 kyr, and the

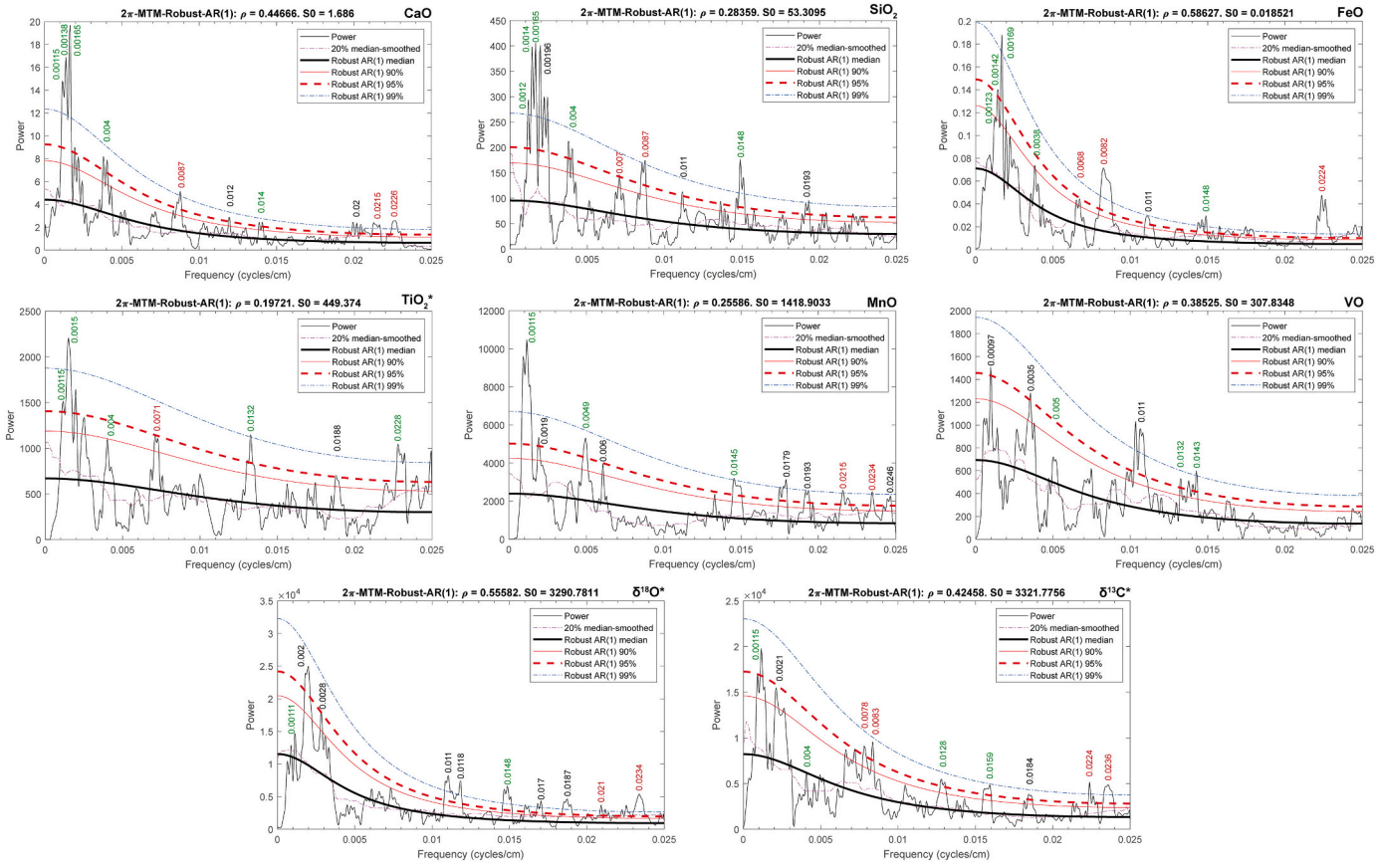

Fig. 4. The 2π-MTM power spectra of the time series of the Vár-hegy section with frequencies of the dominant periodicities. Green color denotes the frequencies of real cycles, red denotes the frequencies of the questionable cycles, and black denotes those peaks which, as shown by other tests (e.g. evolutionary spectra), belong to the background noise or appear shifted along the X-axis and do not represent the true frequency of the cycles. The power spectra of the $\delta^{13}C$ and $\delta^{18}O$ time series were generated after the first outlier removal, and the TiO_2 time series with data replacement. (For interpretation of the references to colour in this figure legend, the reader is referred to the web version of this article.)

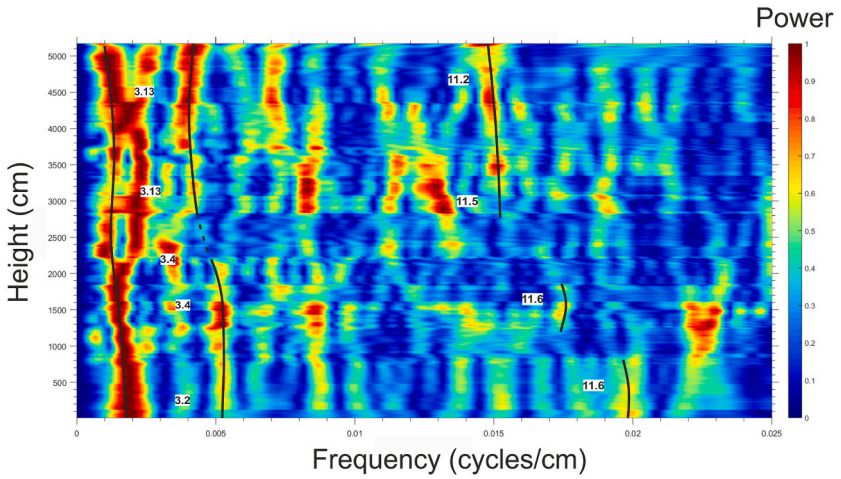

Fig. 5. Evolutionary spectra of the SiO_2 time series. The dominant cycles are marked with black lines and their frequency ratio to the lowest frequency cycle is indicated next to them. The frequency ratio of the 405, 124 and 34 kyr Milankovitch cycles is 1:3.2:11.9. Note the fragmentation of the highest frequency cycle that nevertheless maintains the ratio.

Table 1
Suggested matching of the detected periodicities with the Milankovitch cycles using the ratio method after equating the lowest frequency with the long eccentricity cycle.

Dominant frequencies (cycles/cm)	Period (cm)	Time (kyr)	Milankovitch cycle (kyr)	Milankovitch cycle
0.00133	751.8797	**If 405**	405	Long eccentricity
0.00415	240.9639	129.7952	124	Short eccentricity
0.015	66.6667	35.91	34	Obliquity

periodicity of 0.021–0.023 cycles/cm would translate to a period of 23.5–25.6 kyr. The former differs significantly from the 94 kyr short eccentricity, so it is unlikely to represent a Milankovitch cycle, it may arise from the 50–70 kyr modulation of precession (Yao and Hinnov, 2019). Although the latter one is close to the ~17–21 kyr precession cycle, it is a rather weak signal that is unlikely to represent the precession. If it were a real cycle, then it would belong to a less dominant obliquity cycle with an approx. 25 kyr period. Precession is probably below the detection limit due to the 20 cm sample spacing. Accepting that the frequency of 0.00133 cycles/cm represents the long eccentricity cycle, then precession cycles should appear at approx. 0.026 and 0.032 cycles/cm frequencies, which are only marginally higher than the Nyquist frequency (0.025 cycles/cm) in this study of the Vár-hegy section. As the Nyquist frequency is the reciprocal of twice the sample spacing, precession would only be detectable using a sample spacing of 15 cm that would increase the detection limit to 0.033 cycles/cm. As the precession remains undetectable, there is a risk of aliasing but the difference between the ideal and the actual sample spacing is so small that its influence is negligible, effectively offset by the averaging effect of bioturbation and homogenization during the pulverization of cm-sized rock samples (Weedon, 2003).

The apparent lack of a cycle of ~95 kyr that would belong to the short eccentricity is unexpected, since the commonly less dominant short eccentricity cycle, with a period of ~124 kyr, is present in the signal. If the frequency for long eccentricity is 0.00133 cycles/cm, then the 95 kyr cycle is expected to appear at 0.0057 cycles/cm. There appears some weak and fragmented signal at this frequency but it cannot be confidently identified as a real cycle. Notably, other studies of Triassic-Jurassic boundary sections also found only one frequency peak that belongs to the short eccentricity (Bonis et al., 2010; Deenen et al., 2010; Weedon et al., 2019).

Filtering is based on the cycle and time series with the best-preserved signal which here is identified as the frequency of 0.00133 cycles/cm in the CaO and SiO_2 time series, that yielded the best results overall, and is interpreted to represent the long eccentricity cycle. The FeO and TiO_2 data series yielded similar but slightly noisier results. Even noisier is the signal of the $\delta^{18}O$ and $\delta^{13}C$ time series that may be accounted for their sensitivity to diagenetic overprint (Weedon, 2003). The MnO and VO time series yielded the lowest quality but still interpretable results, where poor quality may be explained by the 28 and 68 missing data points and the commonly almost one order of magnitude lower concentration of these two elements (Table S1). For this reason we refrained from drawing exact conclusions from the results of the MnO and VO time series.

The filtered signals of the highest quality CaO and SiO_2 time series show good agreement, although in antiphase (Fig. 6). We fitted the 405 kyr cycle to the minima in the CaO and to the maxima in the SiO_2 signal. The resulting age models suggest 2901.455 kyr for the deposition of the entire succession on the basis of the CaO signal and slightly more, 2950.254 kyr on the basis of the SiO_2 signal. In addition to these two time series, filtering was also performed on the FeO, TiO_2, and $\delta^{18}O$ time series, whereas the other studied time series were too noisy for acceptable results. The filtered FeO and TiO_2 signals show good agreement with SiO_2 but the filtered signal of $\delta^{18}O$ appear less reliable due to the lower quality of its raw data. In addition, compared to FeO and TiO_2, $\delta^{18}O$ is more in phase with CaO. These relationships are also supported with coherence and phase analysis (Figs. S1–S8). In summary, all filtered time series reveal a total duration of deposition of the studied succession of between 2.9 and 3 Myr (Table 2).

The 2.9–3 Myr total duration of deposition for the entire 51.8 m thick succession translates into an average sedimentation rate of 17.26–17.86 m/Myr (or 1.73–1.79 cm/kyr) for the Vár-hegy section. In the lower part of the succession the sedimentation rate is somewhat lower, e.g. the thickness of the lowermost complete cycle in both the SiO_2 and CaO signal is 680 cm. Equating this to a period of 405 kyr yields a sedimentation rate of 1.68 cm/kyr. In contrast, the thickness of the last complete 405 kyr cycle in both signals is 760 cm which translates into a sedimentation rate of 1.88 cm/kyr. Change in the sedimentation rate detected in the evolutionary spectra is supported by the SiO_2 time series. In the lower part of the section, the distance of adjacent minima is 6.2–6.4 m, it increases to 7.6–7.8 m between 25 and 32 m, and higher up it decreases slightly to 7.2–7.4 m.

COCO analysis also yields 1.7–1.9 cm/kyr as the most likely sedimentation rate and confirms the presence of four Milankovitch cycles, most likely the two eccentricity and two obliquity cycles detected (Fig. 7

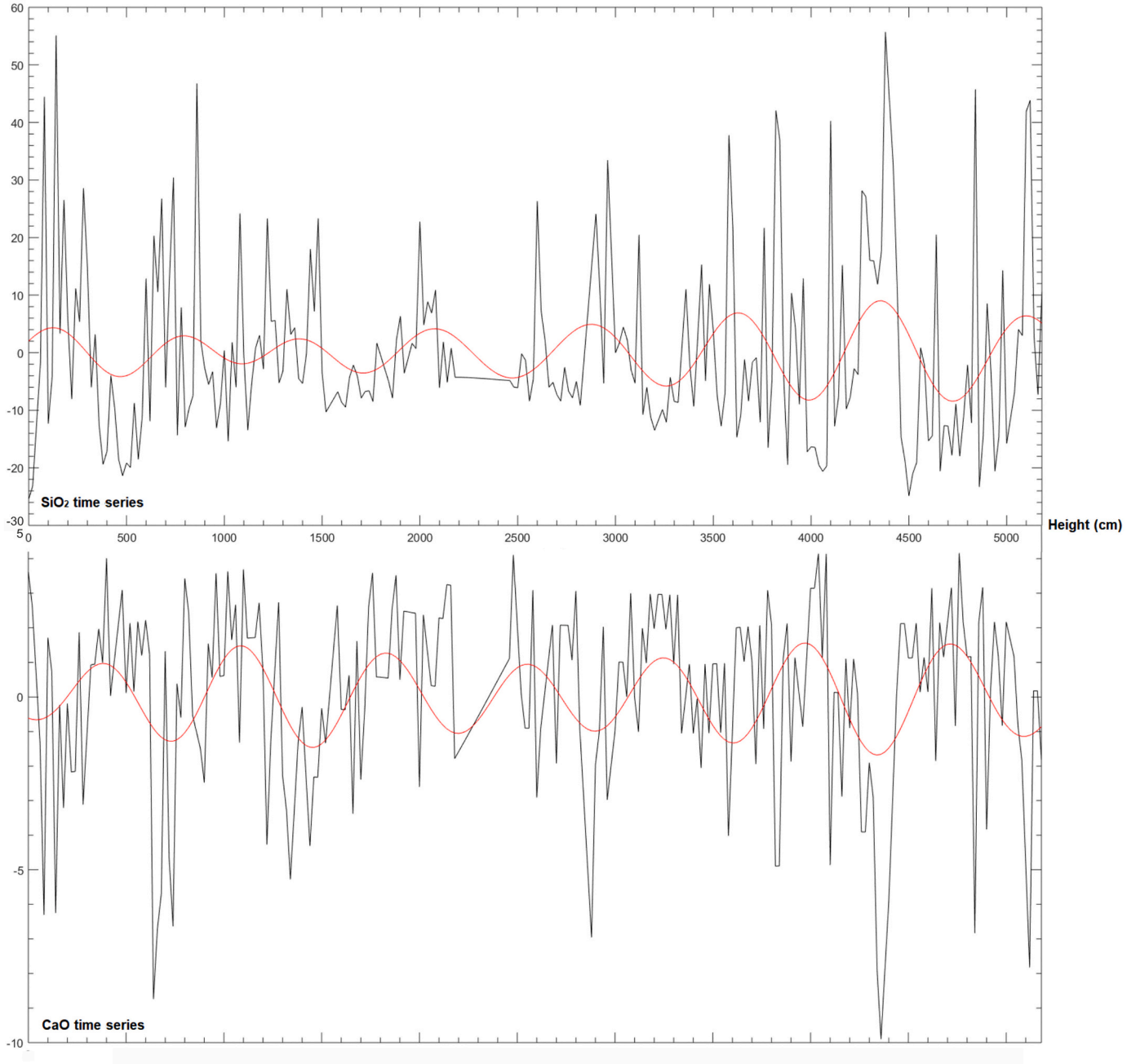

Fig. 6. Filtered CaO and SiO_2 time series, using a Gaussian filter on the cycle with 0,00133 ± 0,00027 cycles/cm frequency. Note that the observed cyclicities are in antiphase with each other.

Table 2
Total duration of deposition of the studied section at Csővár calculated from the filtered time series. The font of the top row indicates the quality of the results of filtering: high (**bold**), acceptable (normal). The durations of the middle row were calculated with the 405 kyr cycle fitted to maxima and the durations in the lowest row were calculated with the 405 kyr cycle fitted to minima.

Time series:	**CaO**	**SiO_2**	**FeO**	**TiO_2**	$\delta^{18}O$
Year:	2,901,614	2,950,254	3,008,864	2,906,471	2,815,074
Year:	2,901,455	2,972,850	2,995,147	2,924,519	2,880,091

and Fig. S9). The eCOCO analysis, whose strength is the detection of changes in the sedimentation rate, also points to somewhat lower sedimentation rate in the lower part of the succession relative to the upper part (Fig. 7 and Fig. S9).

Wavelet analysis revealed 709 and 250 cm cycles in both the SiO_2 and CaO time series and an additional 69 cm cycle in the SiO_2. These are in good agreement with the previously recognized cycles, considering the overall less accurate results of this method. Wavelet analysis confirms a continuous decrease in the frequency associated with the presumed long eccentricity in the lower part of the succession and, significantly, does not reveal any gaps in the succession (Fig. 8 and Fig. S11).

4.3. *Detection of precession in an auxiliary dataset*

Although the original sample spacing in this study was proved to be somewhat wider than required for unambiguous detection of the precession signal, additional spectral analysis was performed on a previously published, more densely spaced $\delta^{18}O$ and $\delta^{13}C$ dataset from a short

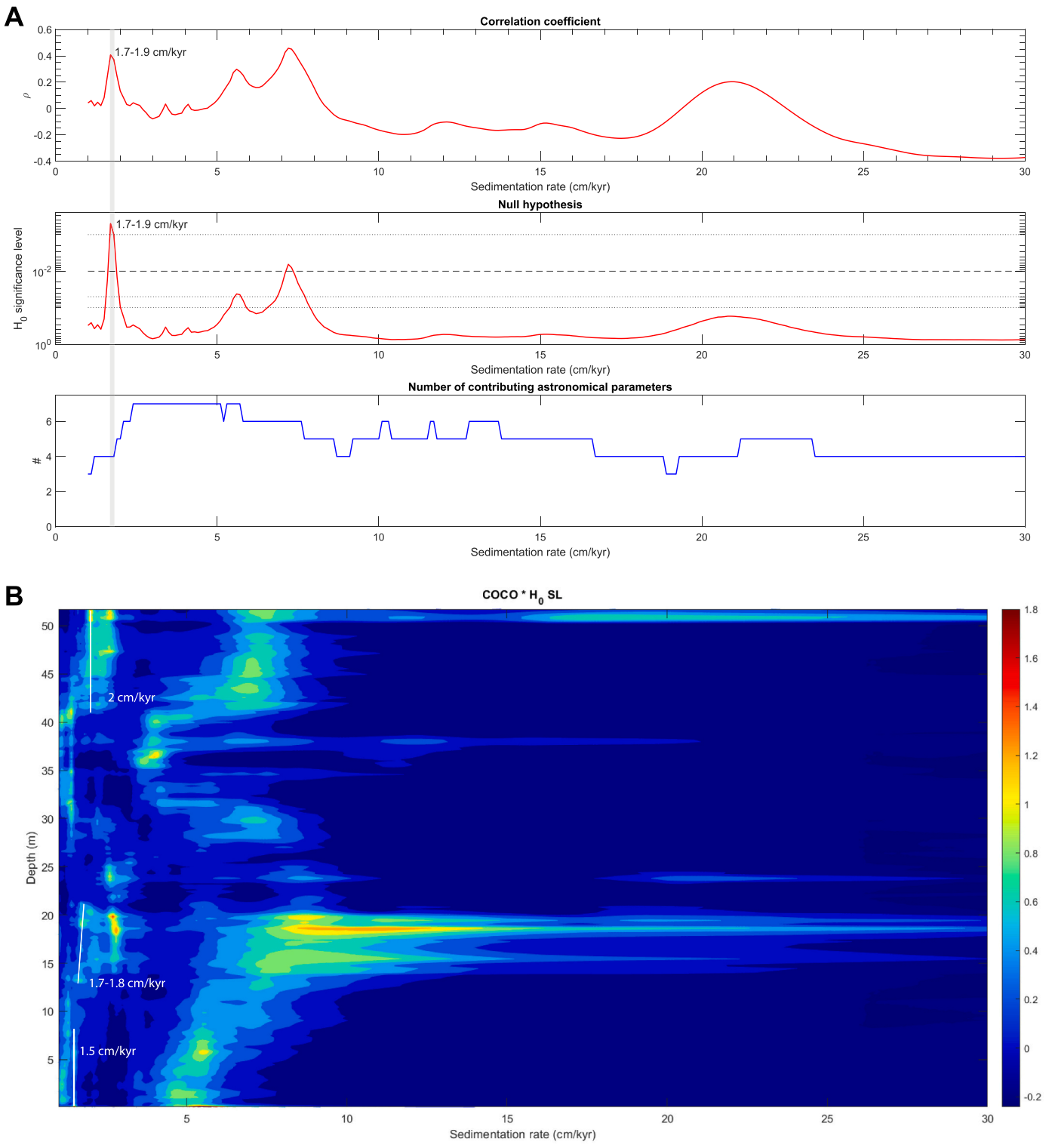

Fig. 7. Result of the COCO (Panel **A**) and eCOCO (Panel **B**) analysis of the CaO time series. On Panel **A** the most probable sedimentation rate suggested by the COCO method is highlighted with grey line, whereas the sedimentation rate change can be seen on the eCOCO plot (white lines and sedimentation rate values).

parallel section within the TJ transition interval, referred to as Section B (see Pálfy et al. (2007) for details and data). As the total thickness of this section is only 3 m, obliquity is the largest cycle that can be detected here. Interpolation to 10 cm spacing was necessary as the original sampling was non-uniform. An additional complexity is that Section B represents an interval near the ICIE where the sedimentation rate is not constant. Nevertheless, the spectral analysis reveals two significant periodicities at ~0.013–0.015 cycles/cm and ~0.026 cycles/cm. In addition, two weak periodicites occur at frequencies of ~0.034 and ~0.04 cycles/cm (Fig. 9).

As demonstrated by the results from the main section, the two precession cycles would be expected around 0.026 and 0.032 cycles/cm, whereas the dominant frequency of obliquity is 0.015 cycles/cm. These values are in broad agreement with the results obtained from Section B, even though the expected frequency of precession was derived from an interval in the main section above Section B where the sedimentation

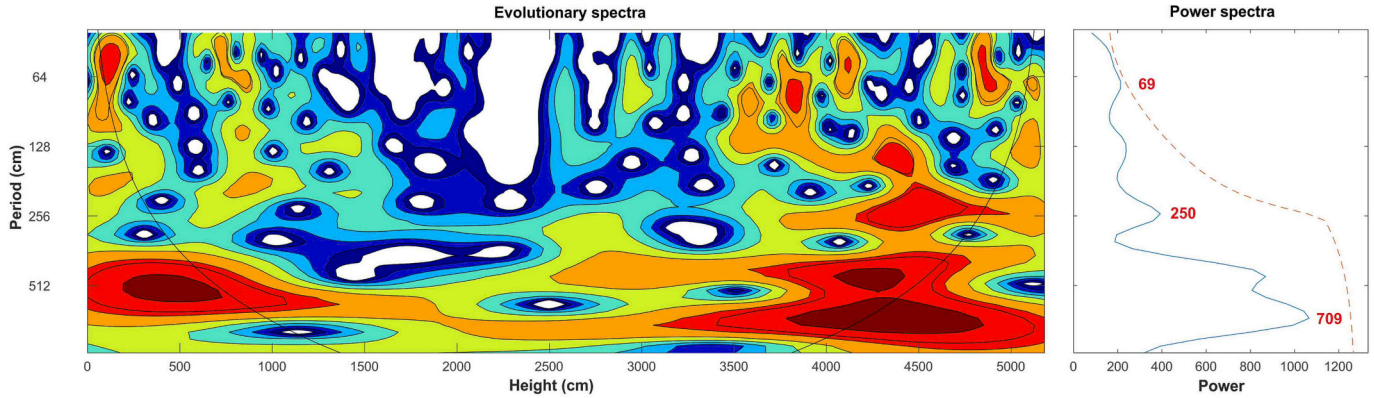

Fig. 8. Evolutionary spectra (left) and power spectra (right) of wavelet analysis on the SiO_2 time series. Note the pronounced frequency change at approx. 1900 cm in the period band between 500 and 700 cm. The white vertical band at approx. 2300 cm results from the unsampled slump deposit (Bed 59).

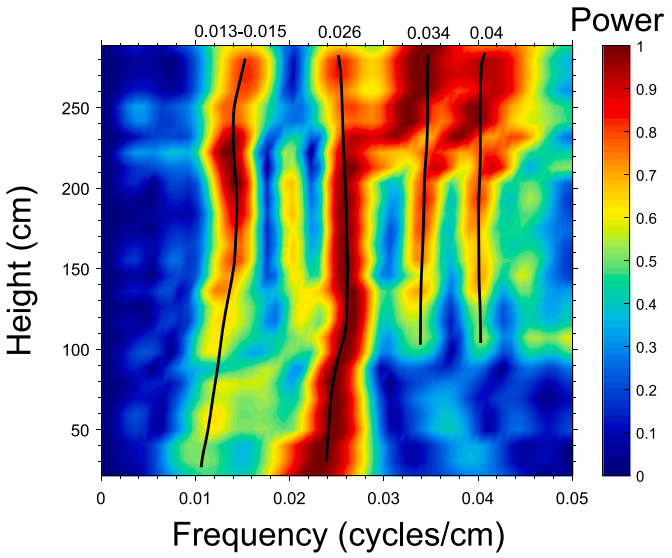

Fig. 9. Evolutionary spectra of the $\delta^{18}O$ time series from Section B at Vár-hegy, Csővár (Pálfy et al., 2007), with the significant periodicities marked.

rate is stable. As the frequency of the long eccentricity cycle in the correlative segment of the main section (Beds 42–55) does not differ from that in the higher part (~0.0014 and 0.00133 cycles/cm), it is reasonable to assume that the frequencies of ~0.026 and ~0.034 cycles/cm in Section B indeed represent the two dominant cycles of precession, i.e. ~21 and 17 kyr near the TJB.

5. Discussion

5.1. *Environmental drivers of Milankovitch cycles preserved in the Csővár sedimentary succession*

As demonstrated by the detected slight differences in the cyclic pattern of the CaO and the other elements, such as the weaker obliquity signal in the CaO time series (Fig. 4), the other five elements are not only passively respond to the dilution effect by the changing CaO content but themselves actively respond to the orbital forcing. The elemental time series of SiO_2, FeO, and TiO_2 represent proxies of terrigenous influx (Westphal et al., 2010; Li et al., 2019b) and are clearly in phase with each other. CaO is in antiphase with these terrigenous proxies and thought to reflect carbonate production and export into the basin, and thus an inverse proxy relative to the terrigenous elements (Sinnesael et al., 2016). The maximum of a long eccentricity cycle is expected to lead to large amplitude oscillations, and conversely, the minimum of a long eccentricity cycle to small oscillations in the signal (Berger and Loutre, 1994; Hinnov and Hilgen, 2012; Hinnov, 2013). Here, the long eccentricity maxima of the filtered CaO time series show small amplitude changes in the signal, whereas the long eccentricity minima of CaO show much larger oscillations (Fig. 6). Consequently, the filtered SiO_2 signal reveals the true phase of long eccentricity, whereas the CaO signal is inverted.

The opposite but correlated changes of terrigenous influx and carbonate production and transportation played the largest role in the preservation of the Milankovitch cycles in the Csővár time series. Correlation is high between the terrigenous proxy elements and the results of the coherence and phase analyses also confirm their similar behaviour. The correlation coefficient of CaO and these elements ranges from −0.5 to −0.7 and thus points to an inverse response of carbonate production and transportation and terrigenous influx to orbital forcing (Table 3).

Remarkably, the difference in correlation coefficient values of SiO_2 suggest that this proxy is not a simple recorder of terrigenous influx but it may also reflect, to some degree, biogenic silica production (e.g. by radiolarians) or diagenetic processes (e.g. silicification). However, high correlation coefficient value with Al_2O_3 (Table 3) and the results of the coherence and phase analyses (Figs. S1–S8) indicate that terrigenous influx is nevertheless a major factor in the SiO_2 data series.

Thus the environmental interpretation of the observed Milankovitch cycles must explain the alternating states of increase in detritally derived elements with a synchronous decrease in Ca content and vice versa. Coherence and phase analyses demonstrate that these two states are in antiphase on the scales of long and short eccentricity and obliquity, so in all likelihood they behave similarly at the scale of precession, too. We speculate that the two alternating states are in fact linked to precession and modulated by the longer cycles such as eccentricity.

During the maximum of seasonality, i.e. when the boreal summer

Table 3
Relative correlation coefficients of CaO and the elements considered as proxies for terrigenous influx. Grey highlights denote the elements used in the cyclostratigraphic analysis for their sufficient data density.

Al_2O_3	1						
SiO_2	0.75579	1					
K_2O	0.80892	0.60308	1				
TiO_2	0.65885	0.42209	0.67376	1			
FeO	0.53208	0.44574	0.48685	0.49387	1		
Rb_2O	0.76255	0.49852	0.83765	0.61417	0.51679	1	
CaO	-0.61237	-0.82792	-0.50468	-0.39489	-0.53113	-0.51621	1
	Al_2O_3	SiO_2	K_2O	TiO_2	FeO	Rb_2O	CaO

occurs at perihelion, the climate extremes become more pronounced (Berger and Loutre, 1994; Hinnov and Hilgen, 2012; Hinnov, 2013), the temperature difference between the continents and the oceans increases and strengthens the "megamonsoon" system that characterized the climate regime during the existence of Pangea (Fig. 10) (Crowley and Baum, 1992; Parrish, 1993; Kutzbach, 1994; Kutzbach and Gallimore, 1989; Bonis et al., 2010). In Late Triassic time the entire peri-Tethyan region was under the influence of the monsoon (Crowley and Baum, 1992; Kutzbach, 1994; Mutti and Weissert, 1995; De Wever et al., 2014) that brought heavy rainfalls in the summer thus intensively flushed the islands assumed to have existed around the Csővár basin (Haas et al., 2010). However, in winters the wind from the dry interiors of the Pangea supercontinent intensified and carried eolian terrigenous dust into the basin (Kutzbach, 1994; Haas et al., 2010; Ruhl et al., 2010; Sinnesael et al., 2016; Budai et al., 2017).

Cyclic thickness variations in early Mesozoic Panthalassan pelagic radiolarites are thought to reflect cyclic changes in continental weathering caused by orbitally forced variations in monsoon intensity (Ikeda et al., 2017, 2020). During stronger monsoonal conditions, the continental weathering of silicate rocks intensifies, which increases the riverine influx of dissolved silica into the ocean, where radiolarians and other siliceous groups benefit from the increased availability. In the present-day, volcanic rocks are exposed at ~10% of the continental landmass experiencing monsoonal rainfalls, yet this area account for 70% of the dissolved silica delivery to the oceans (Hartmann et al., 2014). In the Late Triassic–Early Jurassic, the Emeishan, Siberian and Wrangellia LIPs (and later the newly produced CAMP basalts) were likely all exposed to monsoonal rainfalls so this proportion was likely much higher at that time (Ikeda et al., 2017). In addition to primary differences in biogenic silica content, the diagenetic effects of secondary silica migration was found to enhance the cyclic signal in radiolarian cherts (Ikeda et al., 2017, 2020). During diagenesis the beds with already lower silica content lost silica that migrated into the beds with an already high silica content. Also early diagenetic processes often preserve the silica content in place, hindering the further migration of silica (Hesse and Schacht, 2011). As for the Csővár basin, the main biogenic silica producers were also radiolarians; therefore, similar processes are thought to have controlled the cyclic signal in the SiO_2 time series.

The biosiliceous sediment from radiolarian blooms and the terrigenous detritus could have passively diluted the carbonate content, but carbonate production may also have reacted actively to these effects. The carbonate accumulated in the Csővár basin was mainly derived from the nearby platforms and upper slopes of adjacent islands and submarine highs via calciturbidites (Haas and Tardy-Filácz, 2004; Haas et al., 2010). Modern observations suggest that monsoon precipitation alone, or amplified by increased terrestrial runoff, can reduce the salinity of the surface waters by a few permil (Mutti and Weissert, 1995; Shankar and Shetye, 1999). In concert with decreased light penetration due to the abundance of suspended detritus and strongly changing sea surface

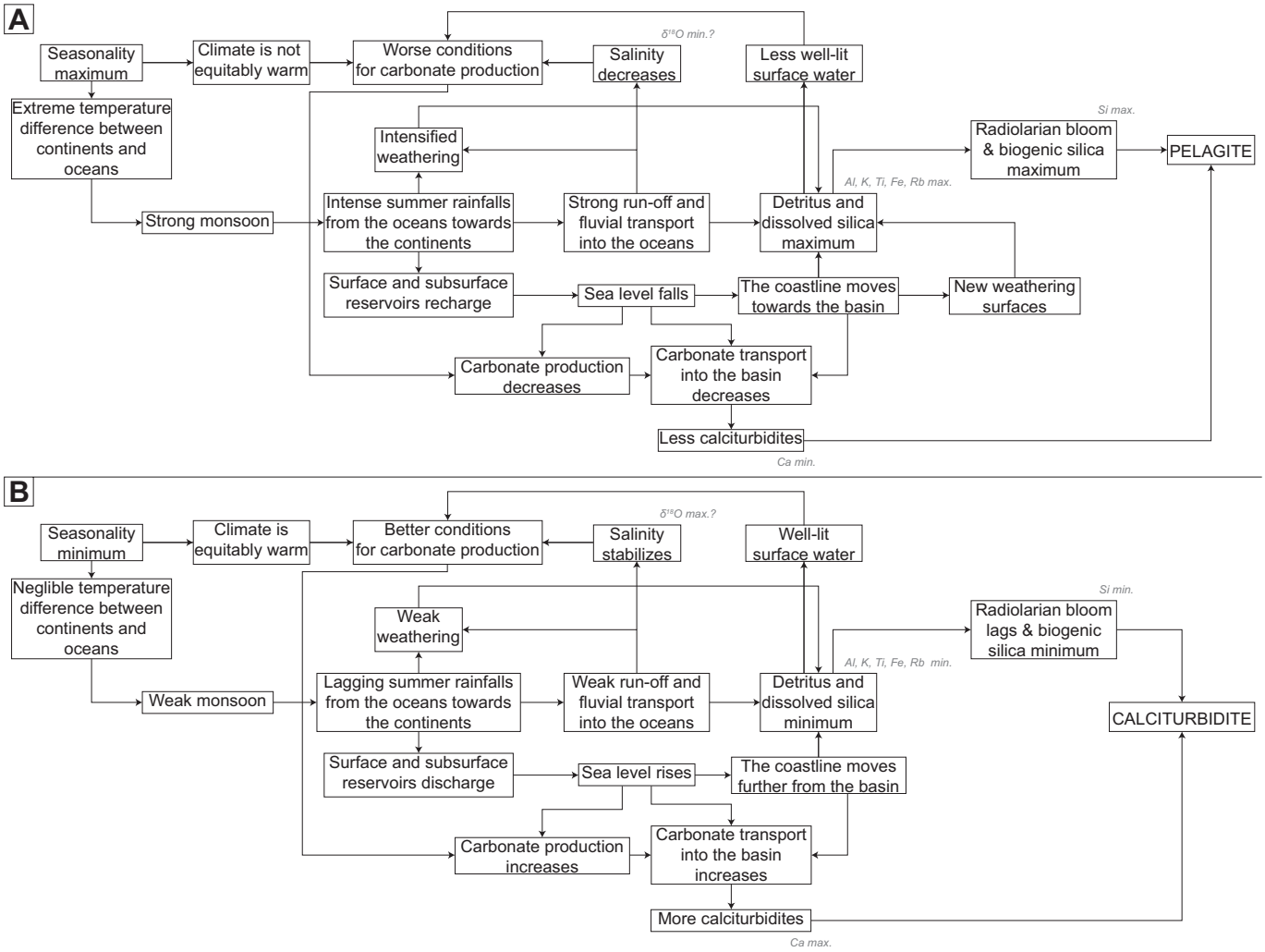

Fig. 10. Conceptualized effects of an intensified monsoon system at the maximum of seasonality (A) and a significantly weakened monsoon system at the minimum of seasonality (B) in the Csővár basin and their preservation in proxy signals.

temperatures, these may have led to a decrease in shallow marine carbonate production (Martínez-Braceras et al., 2017).

Maxima of seasonality thus may have coincided with maxima in terrigenous element supply, including Si, while at these intervals the Ca delivery was reduced. The maxima of the terrigenous components also broadly coincide with the minima in $\delta^{18}O$; the latter possibly record the effects of higher precipitation rates, more intense run-off and increased freshwater input that slightly lowers the salinity in shallow marine areas of carbonate precipitation (Martínez-Braceras et al., 2017).

During minimum seasonality (i.e. when the boreal summer occurs at aphelion), the climate becomes more equitable (Berger and Loutre, 1994, Hinnov and Hilgen, 2012, Hinnov, 2013), which leads to significant weakening of the monsoon system (Fig. 10) (Kutzbach, 1994; Bonis et al., 2010). In turn, this can lead to reduced terrigenous and dissolved silica influx from continental runoff (Kutzbach, 1994), hence failure of the radiolarian blooms (De Wever et al., 2014). Lower accumulation rates of biosiliceous sediment and terrigenous components passively increased the relative carbonate content; this process was possibly actively amplified by the warm, well-lit and normal salinity surface waters that favored biogenic carbonate production (Martínez-Braceras et al., 2017). Thus, the intervals of minimum seasonality coincide with the minima of Si and terrestrial elements and the maxima of Ca, as well as higher $\delta^{18}O$ values perhaps related to the balanced salinity of the marine surface waters (Martínez-Braceras et al., 2017).

The Milankovitch cycles preserved in the signals of $\delta^{13}C$, MnO, and VO are rather weak and noisy, making it difficult to compare them with the other obtained time series. For the latter two, this is likely caused by too many missing data points and lower overall concentration, whereas noise in the carbon isotope record may be related to diagenetic overprint as well as the carbon cycle perturbations in the TJB interval induced by CAMP volcanism. $\delta^{13}C$ and VO probably also reach their maxima at the minimum of seasonality, whereas MnO might be in antiphase with them. The cyclic changes in $\delta^{13}C$ values may be driven by changes in the nutrient supply and primary productivity (Kukert and Riebesell, 1998; Nützel et al., 2010; Martínez-Braceras et al., 2017). Mn and V are redox sensitive elements that may be related to the grade of bottom water oxygenation and, to some degree, may have been also sourced from terrigenous influx (especially Mn). During times of minimum seasonality, when possible monsoon-induced upwellings stalled (De Wever et al., 2014), water column stratification may have developed more easily, which could have facilitated the formation of oxygen-depleted bottom waters. Weak preservation of the Milankovitch cycles in these proxies may reflect differing degrees of water column stratification and the extent of dysoxia during each minimum (Westphal et al., 2010; Martínez-Braceras et al., 2017).

Filtering results are used here to determine where the long eccentricity maxima and minima occur in the succession (Table 4). A comparison of their position with the results of microfacies analysis (Haas and Tardy-Filácz, 2004) provides a sedimentological context to support the model for the origin of cyclicity outlined above. Near long eccentricity maxima, seasonality can reach its absolute maximum (Martínez-Braceras et al., 2017), more argillaceous beds occur at several levels, as in Beds 31, 52, 71, and 88. In proximity of three of the other four eccentricity maxima (in Beds 4, 101, 118 and 121), chert nodules are present, reflecting the abundance of radiolarian-derived biogenic silica. Twenty out of the 33 layers richest in radiolarians (Beds 1, 4–6, 17–20, 22, 31–32, 52, 59, 69, 72, 89, 104, 119, 122–123) also occur near such maxima.

5.2. *Sequence stratigraphic interpretation*

Our cyclostratigraphic results allow for the refinement of a previously developed sequence stratigraphic framework (Haas and Tardy-Filácz, 2004, Haas et al., 2010) (Fig. 11). The oldest four long eccentricity maxima occur consistently close to the very beginning of the transgressive phase of the meter-scale sequences, and the first three long eccentricity minima also consistently appear near the maximum flooding zones (mfz) or during the highstand systems tracts (HST). However, this relationship appears to break down following the initial carbon isotope anomaly (ICIE). Above the level of ICIE, the next long eccentricity minimum (fourth minimum) appears associated with the middle of the transgressive systems tract (TST) and the following maximum (fifth maximum) is near to the level of maximum flooding. The fifth minimum and the sixth maximum appear in similar positions as below the ICIE, before the sixth minimum and the seventh maximum occurs once again during the lower half of the TST and around the mfz. Lastly, the youngest pair of long eccentricity minimum and maximum are in the expected positions. We speculate that the loss of correlation may have been caused by two pairs of missing beats in the sequence stratigraphic record. This may have happened either due to the fundamental environmental and climatic changes (including global warming) during the end-Triassic events or the large-scale transgressive trend and basin

Table 4
Stratigraphic position of maxima (in dark grey) and minima (in light grey) of long eccentricity derived from the four best preserved proxy time series, with the first column showing the integrated results. Note the stabilization of the sedimentation rate from c. 2500 cm that is reflected in less scatter in the results.

Most probable Bed No.	CaO		SiO_2		FeO		TiO_2	
	min./max. (cm)	Bed No.	min./max. (cm)	Bed No.	min./max. (cm)	Bed No.	min./max. (cm)	Bed No.
1–3	40	1	120	3	120	3	20	1
9–12	380	9	460	12	440	12	340	9
18–22	720	20	800	22	760	21	680	18
29	1100	29	1100	29	1100	29	1000	27
33–38	1460	38	1380	34	1460	38	1340	33
43–46	1840	46	1720	44	1840	46	1700	43
55–59	2200	59	2080	56	2200	59	2060	55
60–61	2560	61	2480	60	2540	61	2460	60
70	2900	70	2880	70	2860	70	2880	70
80	3240	80	3260	80	3200	79	3280	80
87	3600	87	3620	87	3540	86	3660	87
91	3960	91	3980	91	3920	90	4020	92
102	4340	102	4340	102	4260	101	4360	102
106–109	4720	109	4720	109	4640	106	4700	108
117–120	5100	120	5100	120	4980	117	5040	117

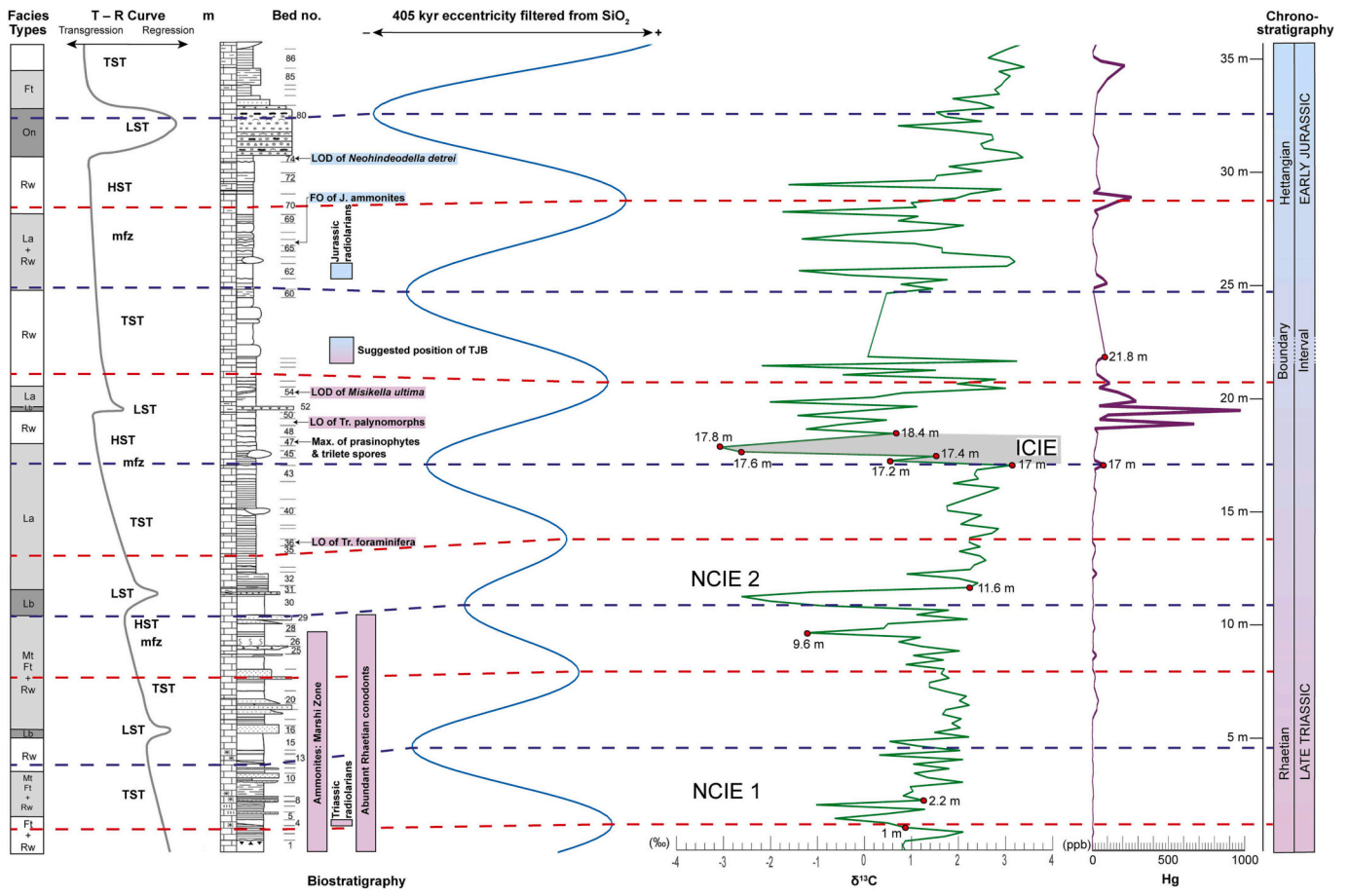

Fig. 11. The lower 37 m of the Vár-hegy section. The figure shows the microfacies, the sea level changes sequence stratigraphically determined by facies changes, the lithologic log (based on Haas and Tardy-Filácz, 2004, Haas et al., 2010), biostratigraphy (purple color denotes the Triassic whereas blue indicates the Jurassic fossils) (Kozur and Mostler, 1990; Pálfy and Dosztály, 2000; Pálfy et al., 2001; Pálfy et al., 2007; Götz et al., 2009; Haas et al., 2010; Karádi, 2018; Karádi et al., 2019), the 405 kyr eccentricity curve filtered from the SiO_2 time series, and the carbon isotope and Hg curves (Kovács et al., 2020). The gray area indicates the location and length of the initial carbon isotope excursion (ICIE). Ft: fine-grained turbidite, Mt.: medium-grained turbidite, Rw: radiolarian wackestone, La: calcisiltite-calcilutite laminate, Lb: lithoclastic-bioclastic grainstone/packstone, On: oncoid, grapestone, grainstone/packstone/wackestone. The key for lithology is the same as in Fig. 2 in Haas et al. (2010). (For interpretation of the references to colour in this figure legend, the reader is referred to the web version of this article.)

deepening identified by Haas and Tardy-Filácz (2004) and Haas et al. (2010).

Thus, sea level variations in the Csővár basin were clearly linked with the long eccentricity cycle and possibly also with all other Milankovitch cycles as Haas et al. (2010) also identified smaller-scale cycles in radiolarian-rich pelagite-calciturbidite variations. However, a clear relationship between sea level and orbitally-forced sedimentary cycles should not necessarily be expected during the Triassic and Jurassic periods. According to Bonis et al. (2010), marked sea level changes at the Triassic-Jurassic boundary have not been caused by either precession or short eccentricity forcing, in line with the lack of polar ice caps at that time (Olsen and Kent, 1996).

However, possible alternative mechanisms for Milankovitch forcing of sea level changes in greenhouse periods have been proposed (Strasser et al., 2007). Changes in the volume of mountain glaciers (Frakes et al., 1992), thermally-induced volume changes in deep water circulations (Schulz and Schäfer-Neth, 1998), and thermal expansion of the uppermost layer of ocean water (Gornitz et al., 1982) are all plausible explanations but recently aquifer- and limno-eustasy is becoming increasingly accepted as a potent driving force of sea level variations in ice-free periods of our planet. Studies showed that the water-bearing potential of groundwater aquifers and lakes is about equal to that of polar ice caps (Southam and Hay, 1981; Hay and Leslie, 1990; Wagreich et al., 2014; Peters and Husson, 2015; Wendler et al., 2016). Aquifer- and limno-eustasy continuously redistributes water between the oceans and continents. During maximum of seasonality the hydrological cycle strengthens and the monsoon delivers water from the oceans to the continents via precipitation. The continental surface and subsurface reservoirs such as lakes and groundwater aquifers recharge, the water level of the lakes rises while at the same time the global sea level falls. During minimum of seasonality the hydrological cycle and the monsoon weakens and the continental reservoirs discharge via fluvial runoff. This may have led to a lowering of water level in lakes and sea level rise in oceans throughout Earth's past (Wagreich et al., 2014; Li et al., 2016; Wendler et al., 2016; Li et al., 2018a). Several recent studies document the antiphase relationship between sea level and lake water level variations (Wagreich et al., 2014; Li et al., 2018a; Hinnov and Cozzi, 2021), or sea level and continental precipitation variations (Wendler et al., 2016) linked by orbital forcing in the Mesozoic.

Aquifer- and limno-eustasy may not only explain the link between sequence stratigraphy and the Milankovitch cycles but also help to understand the coupled cyclic behavior of CaO, carbonate sedimentology and the depositional model described in 5.1. (Fig. 10). The carbonate deposits in peri- and intraplatform basins such as the Csővár basin are mainly derived from the adjacent platforms as calciturbidites. The frequency, composition and thickness of these calciturbidites depend on the sea level and its variations (Le Goff et al., 2020). The cyclic pattern of the pelagite-calciturbidite alternation in Csővár is likely also linked with

cyclic changes in calciturbidite frequency and thickness driven by cyclic sea level variations (Haas and Tardy-Filácz, 2004; Haas et al., 2010).

High sea levels facilitate, whereas low sea levels hinder the transport of platform-derived carbonate into the basins (Harris and Goldhammer, 1987; Reijmer et al., 1994; Le Goff et al., 2020). During high sea levels the rate of carbonate production also rises (Schlager, 1992) and the calciturbidites are more common but thinner (le Goff et al., 2020). When the sea level falls, calciturbidites become more scarce but thicker. Commonly these periods are characterized by basinal deposits in these environments (le Goff et al., 2020).

According to the model described in 5.1., seasonality maxima were associated with low CaO content and high terrigenous element and SiO_2 content. The processes of aquifer- and limno-eustasy predicts that these intervals were characterized by sea level lowstand that led to lower rates of carbonate production and calciturbidite frequency. Also as the coastline moved basinward, the terrigenous influx increased and conditions for carbonate production deteriorated. Overall, seasonality maxima corresponded to deposition of pelagites.

Seasonality minima, on the other hand, were characterized by elevated CaO and reduced terrigenous element and SiO_2 content. Aquifer- and limno-eustasy dictates that these intervals were associated with sea level highstand and a higher rate of carbonate production and increased calciturbidite frequency. As the coastline moved landward, the terrigenous influx reaching the basin decreased. Overall, seasonality minima were therefore characterized with the deposition of calciturbidites.

In summary, the simple model outlined in 5.1. for the orbitally-driven monsoonal climate cycles that control the geochemical signals can be enhanced by the addition of sea level control on the sedimentary record. Combining the results of cyclostratigraphy with sequence stratigraphic interpretation provides new insights into the sedimentary regime of this intraplatform basin and highlights the effects of the end-Triassic events.

5.3. Ramifications of the astrochronologic age model

5.3.1. Duration of the initial carbon isotope anomaly

One of the unresolved issues of TJB studies is the duration of the initial carbon isotope anomaly (ICIE) that is closely associated with the ETE. The carbon isotope data reported by Kovács et al. (2020) was obtained from the same set of samples as used here. Kovács et al. (2020) identified the ICIE between 17 and 18.4 m in the studied section. Although the carbon isotope values start to decrease at 17 m, the most pronounced drop towards negative values appears only at 17.4 m. The termination of the anomaly is also somewhat uncertain as the ICIE appears to end at 18.4 m but there is no sample at 18.0 and 18.2 m due to a slump (Fig. 11). The rebound of the carbon cycle, as reflected by the positive shift in carbon isotope values may therefore have occurred earlier but is masked by the slump-related sampling deficiency. Taking a conservative approach, we examined the length of the ICIE considering the different possible start and end points, based on the results of the filtered CaO and SiO_2 time series (Table 5).

Our data (Table 5) is compatible with a minimum duration estimate of ~40 kyr, if the ICIE is located between 17.4 and 18.0/18.2 m in the section. Following the opinion of Kovács et al. (2020) and positioning the ICIE at 17–18.4 m results in a maximum duration estimate of ~80 kyr.

Table 5
Possible length of the initial carbon isotope anomaly at different stratigraphic positions, based on the age model of the CaO and SiO_2 time series.

The position of the Initial carbon isotope anomaly (m)	CaO (kyr)	SiO_2 (kyr)
17–18	54.7	58
17–18.2	65.7	69.5
17–18.4	76.6	81
17.4–18	32.8	34.7
17.4–18.2	43.8	46.3
17.4–18.4	54.7	57

Constraints from Csővár can be compared with cyclostratigraphic results for the length of the ICIE from other studied sections. Estimates based on the St. Audrie's Bay section (Bristol Channel Basin, UK; Ruhl et al., 2010) and the Newark and Hartford basin successions (Whiteside et al., 2010) suggest a 1–2 precession cycle duration (~21 and 42 kyr) for the ICIE, whereas Deenen et al. (2010) based on Argana Basin (Morocco) continental successions, and Blackburn et al. (2013) based on the Newark and Fundy basin successions, suggest only a one precession cycle duration (~21 kyr). Bonis et al. (2010) also estimate a ~20 kyr duration for the ICIE based on the St. Audrie's Bay succession, while Yager et al. (2017) estimated a 85 ± 25 kyr duration on the basis of zircon U-Pb dates in the Levanto section in Peru.

5.3.2. Timing of other geochemical anomalies and biotic events

Current research has focused on understanding the causes of multiple negative carbon isotope anomalies in the TJB interval, the purported precursor CIE before, and the main CIE after the ICIE (Korte et al., 2019). If NCIE-2 is identified to be the precursor CIE in the Csővár section (Kovács et al., 2020), the age model presented here suggests that it precedes the ICIE (i.e. NCIE-3) by 413 kyr (see Supplementary material, Table S2). The main CIE, as defined in the St. Audrie's Bay section (Hesselbo et al., 2002), is a prolonged anomaly with no analogue at Csővár. Of successive peaks of early Hettangian negative anomalies here, NCIE-4 follows the ICIE by 1170 kyr, whereas elapsed time between both NCIE-4 and 5, and NCIE-5 and 6 is 317 kyr. The pacing of carbon isotope anomalies may be influenced by flare-ups of CAMP volcanic activity.

Elevated concentrations of mercury in sedimentary strata are regarded as proxy for eruptive volcanism; a major peak of [Hg] was indeed found between 17 and 21.8 m, immediately above the ICIE (Kovács et al., 2020). Assuming that the major carbon cycle perturbation was initiated by the first, intrusive phase of CAMP (Davies et al., 2017; Ruhl et al., 2020) and the [Hg] peak resulted from the subsequent eruptive climax, our age model suggests a 58 kyr lag between these phases (Table S2). The major peak and five minor peaks of elevated [Hg] in the lower Hettangian part of the section are separated by strata that represent different intervals ranging from 197 to 317 kyr (Table S2), pointing to irregular pacing of recurrent eruptive activity of CAMP. Ongoing and future geochemical studies of the Csővár section will also benefit from the time frame provided by our astrochronologic age model.

Further insights can be gained from timing of the biotic events recorded in the section. A unique feature is the occurrence of conodonts in the lowermost Hettangian, known only at this locality (Pálfy et al., 2001; Du et al., 2020). Our age model suggests that the last occurrence datum (LOD) of *Misikella ultima* postdates the peak of ICIE by 139 kyr, whereas the LOD of *Neohindeodella detrei* follows the ICIE by 699 kyr (Table S2). At several localities worldwide, including the GSSP at Kuchjoch, the LOD of the last conodonts is correlative with the ICIE (Hillebrandt et al., 2013; Du et al., 2020). Synchrony of marine and terrestrial ecosystem collapse with the most severe carbon cycle perturbation is evidenced by the spore and prasinophyte spike correlative with the ICIE at Csővár (Götz et al., 2009). Our age model constrains the duration of both palynological events to 52 kyr (Table S2). While the *Neohindeodella detrei* conodont biozone can be regarded as the survival interval after the ETE, onset of recovery may be signaled by renewed import of redeposited bioclasts recorded by oncoidal grapestones from 31.2 m that occurred 710 kyr after the peak of the ICIE (Table S2). Furthermore, gradual ecosystem deterioration and the onset of the biotic crisis prior to the ETE may be heralded by the last occurrence of abundant platform-derived carbonate components in the latest Triassic, at 12 m, or 311 kyr prior to the onset of the ICIE, with the LOD of Rhaetian foraminifera (Pálfy et al., 2007) 162 kyr before this datum (Table S2).

5.3.3. Position of the Triassic-Jurassic boundary

The position of the TJB in the Csővár section is only loosely constrained biostratigraphically, to a ~ 6 m interval between Beds 49 and 62, i.e. the LOD of Triassic palynomorphs (Götz et al., 2009) and the FOD of Jurassic radiolarians (Pálfy et al., 2001). The astrochronology developed here is applied for placement of the system boundary by comparison with the GSSP at Kuhjoch and correlation of the ICIE. A recently published cyclostratigraphic analysis uses precession and eccentricity signals in the stratotype section to estimate the duration of the interval between the ICIE (equivalent with the ETE) and the TJB as defined by the FOD of *Psiloceras spelae*, as 270 kyr (Galbrun et al., 2020). Projecting the duration of this interval to the Csővár section from the onset of the ICIE (i.e. locally the NCIE-3), the base of the Jurassic should thus be located between 21.8 and 22.2 m or Bed 58–59, immediately above the end of the major Hg anomaly and within the biostratigraphic constraints described above (Fig. 11).

5.3.4. Duration of the Hettangian stage

Our results bear on the debated duration of the Hettangian, the first stage of the Jurassic. The latest edition ot the most widely used Geological Time Scale (Hesselbo et al., 2020) establishes a stage duration of 1.9 Myr, on the basis of supplementing the 1.8 Myr cyclostratigraphy-based estimate from the St. Audrie's Bay section (Ruhl et al., 2010) with 0.1 Myr for the earliest ammonite zone of the Hettangian. A re-analysis of the same dataset suggests a 1.97 Myr duration (Huang, 2018). These estimates are in agreement with U-Pb calibration of ammonite-constrained sections in Peru (Schaltegger et al., 2008; Guex et al., 2012). However, completeness of the St. Audrie's Bay record was recently questioned and an alternative stage duration estimate of $\geq$4.1 Myr was proposed (Weedon et al., 2019), i.e. more than twice the duration suggested by others.

Adopting the position of the TJB at Csővár as advocated in section 5.3.3., our astrochronology allocates 1.24–1.255 Myr based on the CaO time series and 1.34–1.36 Myr based on the SiO_2 time series to the Triassic, and 1.65–1.66 Myr based on the results of the (based on CaO time series) or 1.6–1.61 Myr (based on SiO_2 time series) to the Jurassic segments of the section. Although the occurrence of *Waehneroceras* near the top of the section was previously used to suggest a middle Hettangian age (Pálfy and Dosztály, 2000), more recent finds including *Schlotheimia* sp. from the the top of the section suggests that it likely extends into the late Hettangian (Kovács et al., 2020). Thus our results are in good agreement with a short (i.e. $\leq$2 Myr) Hettangian but would be hard to reconcile with a doubled stage duration. Additionaly, our age model allows a calculation of the average rate of sedimentation as 17.3–17.9 m/Myr. This is comparable to an analogous Middle Triassic intraplatform basin characterized by calciturbidites in the Dolomites where calibration by U-Pb zircon ages led to calculation of average sedimentation rate of 13.5 m/Myr (Maurer et al., 2004).

6. Conclusions

The continuous marine TJB section at Csővár is of international significance as it has already produced a wealth of important paleontological and geochemical data that helped elucidate the ETE and related environmental change. However, an accurate age model has been lacking so far. Here we used newly obtained high-resolution time series of ten elements and existing stable isotope data for multiproxy cyclostratigraphic analysis that led to the detection of Milankovitch cycles. The ~405 kyr long and ~124 kyr short eccentricity, the ~34 kyr obliquity and later the ~17 and ~21 kyr precession cycles were all identified. Weaker ~61–77 kyr and ~23.5–25.6 kyr cycles were also detected, but the possibility that they arise from the background noise cannot be excluded. If real, the longer cycle most likely corresponds to the 50–70 kyr modulation of precession, whereas the former corresponds to a less dominant obliquity cycle with a ~25 kyr period.

Based on these identified cycles, our astrochronological age model suggests that the ~52 m thick succession was deposited in 2.9–3 Myr that includes the last ~1.3 Myr of the Rhaetian and most of the Hettangian, in agreement with a <2 Myr duration of the first stage of the Jurassic. The average sedimentation rate was 1.73–1.79 cm/kyr that increased gradually and peaked near the TJB, and then remained stable. The age model suggests that the duration of the ICIE is between ~40–80 kyr and allows to place time constraints on various records of biotic and environmental change in the TJB interval, thereby helping to elucidate Earth systems feedbacks within the cascade of events likely triggered by CAMP volcanism.

Our results are in agreement with previous sequence stratigraphic studies. Up to the ICIE, the meter-scale sequences correspond to the ~405 kyr long eccentricity cycles. The transgressive phases of the sequences consistently occur at long eccentricity maxima, whereas their minima correspond to the highstand systems tracts or the maximum flooding zones. After the ICIE this relationship becomes less obvious, likely reflecting the environmental and climatic changes related to the ETE superimposed on the long-term transgression.

We propose a complex environmental model for the Csővár basin, where aquifer- and limno-eustasy are identified as the main drivers of cyclicity. The prevailing "megamonsoon" climate regime resulted in the opposite, antiphase response of the terrigenous input and the carbonate accumulation in the basin. This model may also be applicable to other, similar intraplatform basins.

CRediT authorship contribution statement

Zsolt Vallner: Conceptualization, Methodology, Investigation, Formal analysis, Visualization, Writing – original draft, Writing – review & editing. **Emma Blanka Kovács:** Investigation, Writing – review & editing. **János Haas:** Investigation, Writing – review & editing. **Ferenc Móricz:** Investigation, Resources. **Micha Ruhl:** Writing – review & editing. **Norbert Zajzon:** Resources, Writing – review & editing. **József Pálfy:** Conceptualization, Funding acquisition, Supervision, Writing – original draft, Writing – review & editing.

Declaration of Competing Interest

The authors declare that they have no known competing financial interests or personal relationships that could have appeared to influence the work reported in this paper.

Data availability

All datasets related to this article are included in the Supplementary material.

Acknowledgements

We thank Erzsébet Rábl, Tamás Weiszburg, Boglárka Topa and Fanni Szabó for their help in sample preparation. Dávid Bajnai provided helpful comments on the first author's thesis that formed the basis of this work. Constructive comments of two anonymous reviewers helped to improve the manuscript. Funding from NKFIH OTKA Grants K135309, NN128702, and FK135115 is acknowledged. The research was partly supported by the European Union and the State of Hungary, co-financed by the European Regional Development Fund in the project of GINOP-2.3.2.-15-2016-00009 'ICER'. This is ELKH-MTM-ELTE Paleo contribution No. 369.

Appendix A. Supplementary data

Supplementary data to this article can be found online at https://doi.org/10.1016/j.palaeo.2023.111493.

References

Benkő, K., Fodor, L., 2002. Csővár környékének szerkezetföldtana (Structural geology near Csővár, Hungary). Földtani Közlöny 132 (2), 223–246.

Berger, A., Loutre, M.F., 1994. Precession, eccentricity, obliquity, insolation and paleoclimates. In: Duplessy, J.-C., Spyridakis, M.-T. (Eds.), Long-Term Climatic Variations. NATO ASI Series 22. Springer Berlin, Heidelberg, pp. 107–151. https://doi.org/10.1007/978-3-642-79066-9_5.

Blackburn, T.J., Olsen, P.E., Bowring, S.A., McLean, N.M., Kent, D.V., Puffer, J., McHone, G., Rasbury, E.T., Et-Touhami, M., 2013. Zircon U-Pb geochronology links the end-triassic extinction with the Central Atlantic Magmatic Province. Science 340, 941–945. https://doi.org/10.1126/science.1234204.

Bloomfield, P., 1976. Fourier Analysis of Time Series: An Introduction. — Wiley, London.

Bonis, N.R., Ruhl, M., Kürschner, W.M., 2010. Milankovitch-scale palynological turnover across the Triassic-Jurassic transition at St. Audrie's Bay, SW UK. J. Geol. Soc. 167, 877–888. https://doi.org/10.1144/0016-76492009-141.

Budai, T., Haas, J., Vörös, A., Molnár, Z., 2017. Influence of upwelling on the sedimentation and biota of the segmented margin of the western Neotethys: a case study from the Middle Triassic of the Balaton Highland (Hungary). Facies 63, 22. https://doi.org/10.1007/s10347-017-0504-1.

Crowley, T.J., Baum, S.K., 1992. Milankovitch fluctuations on supercontinents. Geophys. Res. Lett. 19 (8), 793–796.

Davies, J.H.F.L., Marzoli, A., Bertrand, H., Youbi, N., Ernesto, M., Schaltegger, U., 2017. End-Triassic mass extinction started by intrusive CAMP activity. Nat. Commun. 8, 15596. https://doi.org/10.1038/ncomms15596.

Deenen, M.H.L., Ruhl, M., Bonis, N.R., Krijgsman, W., Kuerschner, W.M., Reitsma, M., van Bergen, M.J., 2010. A new chronology for the end-Triassic mass extinction. Earth Planet. Sci. Lett. 291 (1), 113–125. https://doi.org/10.1016/j.epsl.2010.01.003.

De Wever, P., O'Dogherty, L., Goričan, Š., 2014. Monsoon as a cause of radiolarite in the Tethyan realm. C. R. Geosci. 346, 287–297. https://doi.org/10.1016/j.crte.2014.10.001.

De Winter, N.J., Sinnesael, M., Makarona, C., Vansteenberge, S., Claeys, P., 2017. Trace element analyses of carbonates using portable and micro-X-ray fluorescence: performance and optimization of measurement parameters and strategies. J. Anal. At. Spectrom. 32, 1211. https://doi.org/10.1039/C6JA00361C.

Du, Y., Chiari, M., Karádi, V., Nicora, A., Onoue, T., Pálfy, J., Roghi, G., Tomimatsu, Y., Rigo, M., 2020. The asynchronous disappearance of conodonts: new constraints from Triassic-Jurassic boundary sections in the Tethys and Panthalassa. —. Earth-Sci. Rev. 203, 103176 https://doi.org/10.1016/j.earscirev.2020.103176.

Frakes, L.A., Francis, J.E., Syktus, J.I., 1992. Climate modes of the Phanerozoic. In: Cambridge University Press, Cambridge, p. 274 p..

Galbrun, B., Boulila, S., Krystyn, L., Richoz, S., Gardin, S., Bartolini, A., Maslo, M., 2020. "Short" or "long" Rhaetian ? Astronomical calibration of Austrian key sections. Glob. Planet. Chang. 192, 103253 https://doi.org/10.1016/j.gloplacha.2020.103253.

Gornitz, V., Lebedeff, S., Hansen, J., 1982. Global sea-level trend in the past century. Science 215, 1611–1614. https://doi.org/10.1126/science.215.4540.1611.

Götz, A.E., Ruckwied, K., Pálfy, J., Haas, J., 2009. Palynological evidence of synchronous changes within the terrestrial and marine realm at the Triassic/Jurassic boundary (Csővár section, Hungary). Rev. Palaeobot. Palynol. 156 (3–4), 401–409. https://doi.org/10.1016/j.revpalbo.2009.04.002.

Greene, S.E., Martindale, R.C., Ritterbush, K.A., Bottjer, D.J., Corsetti, F.A., Berelson, W. M., 2012. Recognising Ocean acidification in deep time: an evaluation of the evidence for acidification across the Triassic-Jurassic boundary. Earth Sci. Rev. 113 (1-2), 72–93. https://doi.org/10.1016/j.earscirev.2012.03.009.

Guex, J., Schoene, B., Bartolini, A., Spangenberg, J., Schaltegger, U., O'Dogherty, L., Taylor, D., Bucher, H., Atudorei, V., 2012. Geochronological constraints on post-extinction recovery of the ammonoids and carbon cycle perturbations during the Early Jurassic. Palaeogeogr. Palaeoclimatol. Palaeoecol. 346, 1–11. https://doi.org/10.1016/j.palaeo.2012.04.030.

Haas, J., 2002. Origin and evolution of Late Triassic platform carbonates in the Transdanubian Range (Hungary). Geol. Carpath. 53, 159–178.

Haas, J., Budai, T., 1999. Triassic sequence stratigraphy of the Transdanubian Range (Hungary). Geol. Carpath. 50, 459–475.

Haas, J., Götz, A.E., Pálfy, J., 2010. Late Triassic to Early Jurassic palaeogeography and eustatic history in the NW Tethyan realm: New insights from sedimentary and organic facies of the Csővár Basin (Hungary). Palaeogeogr. Palaeoclimatol. Palaeoecol. 291, 456–468. https://doi.org/10.1016/j.palaeo.2010.03.014.

Haas, J., Győri, O., Kocsis, T.Á., Lantos, Z., Pálfy, J., 2018. A triász és a jura időszak határán lezajlott globális krízis és annak nyomai magyarországi rétegsorokban. Földtani Közlöny 148 (1), 9–26. https://doi.org/10.23928/foldt.kozl.2018.148.1.9.

Haas, J., Jovanović, D., Görög, Á., Sudar, M.N., Józsa, S., Ozsvárt, P., Pelikán, P., 2019. Upper Triassic-Middle Jurassic resedimented toe-of-slope and hemipelagic basin deposits in the Dinaridic Ophiolite Belt, Zlatar Mountain, SW Serbia. Facies 65/2, 23. https://doi.org/10.1007/s10347-019-0566-3.

Haas, J., Korpás, L., Török, Á., Dosztály, L., Góczán, F., Hámor-Vidó, M., Oravecz-Scheffer, A., Tardi-Filácz, E., 2000. Felső-triász medence- és lejtőfácies a Budai-hegységben a Vérhalom téri fúrás vizsgálatának tükrében (Upper Triassic basin and slope facies in the Buda Mts. based on study of core drilling Vérhalom tér, Budapest). Földtani Közlöny 130, 371–421.

Haas, J., Tardy-Filácz, E., 2004. Facies changes in the Triassic-Jurassic boundary interval in an intraplatform basin succession at Csővár (Transdanubian Range, Hungary). Sediment. Geol. 168, 19–48. https://doi.org/10.1016/j.sedgeo.2004.03.002.

Haas, J., Tardi-Filácz, E., Oravecz-Scheffer, A., Góczán, F., Dosztály, L., 1997. Stratigraphy and sedimentology of an Upper Triassic toe-of-slope and basin succession at Csővár. Acta Geol. Hung. 40, 111–177.

Harris, T.M., Goldhammer, R., 1987. Platform/foreslope facies and buildup geometry resulting from short-term and long-term eustatic sea level fluctuations: latemar buildup (Middle Triassic), Dolomites, northern Italy. Am. Assoc. Pet. Geol. Bull. 71, 5.

Hartmann, J., Moosdorf, N., Lauerwald, R., Hinderer, M., West, A.J., 2014. Global chemical weathering and associated P-release—the role of lithology, temperature and soil properties. Chem. Geol. 363, 145–163. https://doi.org/10.1016/j.chemgeo.2013.10.025.

Hay, W.W., Leslie, M.A., 1990. Could Possible Changes in Global Groundwater Reservoir Cause Eustatic Sea Level fluctuations? — Sea Level Change: Studies in Geophysics. In: National Academy Press, Washington D.C., pp. 161–170

He, T., Corso, J., Newton, R., Wignall, P., Mills, B., Todaro, S., Stefano, P., Turner, E., Jamieson, R., Randazzo, V., Rigo, M., Jones, R., Dunhill, A., 2020. An enormous sulfur isotope excursion indicates marine anoxia during the end-Triassic mass extinction. Sci. Adv. 6/37, eabb6704. https://doi.org/10.1126/sciadv.abb6704.

Hesse, R., Schacht, U., 2011. Early diagenesis of deep-sea sediments. Dev. Sedimentol. 63, 557–713. https://doi.org/10.1016/B978-0-444-53000-4.00009-3.

Hesselbo, S.P., Ogg, J.G., Ruhl, M., 2020. The Jurassic Period. —. In: Gradstein, F.M., Ogg, J.G., Schmitz, M.D., Ogg, G.M. (Eds.), Geologic Time Scale 2020. Elsevier, pp. 955–1021. https://doi.org/10.1016/B978-0-12-824360-2.00026-7.

Hesselbo, S.P., Robinson, S.A., Surlyk, F., Piasecki, S., 2002. Terrestrial and marine mass extinction at the Triassic-Jurassic boundary synchronized with major carbon-cycle perturbation: a link to initiation of massive volcanism? Geology 30 (3), 251–254. https://doi.org/10.1130/0091-7613(2002)030<0251:tameat>2.0.co;2.

Hillebrandt, A.V., Krystyn, L., Kürschner, W.M., Bonis, N.R., Ruhl, M., Richoz, S., Schobben, M.A.N., Urlichs, M., Bown, P.R., Kment, K., Mcroberts, C.A., Simms, M., Tomašových, A., 2013. The Global Stratotype Sections and Point (GSSP) for the base of the Jurassic System at Kuhjoch (Karwendel Mountains, Northern Calcareous Alps, Tyrol, Austria). Episodes 36/3, 162–198. https://doi.org/10.18814/epiiugs/2013/v36i3/001.

Hinnov, L.A., 2013. Cyclostratigraphy and its revolutionizing applications in the earth and planetary sciences. Geol. Soc. Am. Bull. 125 (11–12), 1703–1734. https://doi.org/10.1130/B30934.1.

Hinnov, L.A., Cozzi, A., 2021. Rhaetian (Late Triassic) Milankovitch cycles in the Tethyan Dachstein Limestone and Laurentian Passaic Formation linked by the g2–g5 Astronomical Metronome. Bol. Geol. Min. 131 (2), 269–290. https://doi.org/10.21701/bolgeomin.131.2.004.

Hinnov, L.A., Hilgen, F.J., 2012. Cyclostratigraphy and astrochronology. In: Gradstein, F. M., Ogg, J.G., Schmitz, M.D., Ogg, G.M. (Eds.), The Geologic Time Scale 2012. Elsevier, pp. 63–83. https://doi.org/10.1016/B978-0-444-59425-9.00004-4.

Huang, C., 2018. Astronomical time scale for the Mesozoic. In: Montenari, M. (Ed.), Stratigraphy & Timescales 3. Academic Press, pp. 81–150. https://doi.org/10.1016/bs.sats.2018.08.005.

Hüsing, S.K., Beniest, A., van der Boon, A., Abels, H.A., Deenen, M.H.L., Ruhl, M., Krijgsman, W., 2014. Astronomically-calibrated magnetostratigraphy of the Lower Jurassic marine successions at St. Audrie's Bay and East Quantoxhead (Hettangian–Sinemurian; Somerset, UK). Palaeogeogr. Palaeoclimatol. Palaeoecol. 403, 43–56. https://doi.org/10.1016/j.palaeo.2014.03.022.

Ikeda, M., Tada, R., 2014. A 70 million year astronomical time scale for the deep-sea bedded chert sequence (Inuyama, Japan): implications for Triassic-Jurassic geochronology. Earth Planet. Sci. Lett. 399, 30–43. https://doi.org/10.1016/j.epsl.2014.04.031.

Ikeda, M., Tada, R., Ozaki, K., 2017. Astronomical pacing of the global silica cycle recorded in Mesozoic bedded cherts. Nat. Commun. 8 (1), 1–9. https://doi.org/10.1038/ncomms15532.

Ikeda, M., Ozaki, K., Legrand, J., 2020. Impact of 10-Myr scale monsoon dynamics on Mesozoic climate and ecosystems. Sci. Rep. 10 (1), 1–10. https://doi.org/10.1038/s41598-020-68542-w.

Jost, A.B., Bachan, A., van de Schootbrugge, B., Lau, K.V., Weaver, K.L., Maher, K., Payne, J.L., 2017. Uranium isotope evidence for an expansion of marine anoxia during the end-Triassic extinction. Geochem. Geophys. Geosyst. 18 (8), 3093–3108. https://doi.org/10.1002/2017GC006941.

Karádi, V., 2018. Middle Norian conodonts from the Buda Hills, Hungary: an exceptional record from the western Tethys. J. Iberian Geol. 44 (1), 155–174. https://doi.org/10.1007/s41513-017-0009-3.

Karádi, V., Cau, A., Mazza, M., Rigo, M., 2019. The last phase of conodont evolution during the Late Triassic: integrating biostratigraphic and phylogenetic approaches. Palaeogeogr. Palaeoclimatol. Palaeoecol. 549, 109144 https://doi.org/10.1016/j.palaeo.2019.03.045.

Karádi, V., Kozur, H.W., Görög, Á., 2013. Stratigraphically important lower Norian conodonts from the Csővár borehole (Csv-1), Hungary – comparison with the conodont succession of the Norian GSSP candidate Pizzo Mondello (Sicily, Italy). In: Tanner, L.H., Spielmann, J.A., Lucas, S.G. (Eds.), The Triassic System: New Mexico Museum of Natural History and Science Bulletin, 61, pp. 284–295.

Kent, D.V., Olsen, P.E., Muttoni, G., 2017. Astrochronostratigraphic polarity time scale (APTS) for the Late Triassic and early Jurassic from continental sediments and correlation with standard marine stages. —. Earth Sci. Rev. 166, 153–180. https://doi.org/10.1016/j.earscirev.2016.12.014.

Kodama, K.P., Hinnov, L., 2015. Rock Magnetic Cyclostratigraphy. — John Wiley and Sons, New York.

Korte, C., Ruhl, M., Pálfy, J., Ullmann, C.V., Hesselbo, S.P., 2019. Chemostratigraphy across the Triassic–Jurassic boundary. In: Sial, A.N., Gaucher, C., Ramkumar, M., Ferreira, V.P. (Eds.), Chemostratigraphy Across Major Chronological Boundaries: AGU Geophysical Monograph Series 240, pp. 185–210. https://doi.org/10.1002/9781119382508.ch10.

Kovács, E.B., Ruhl, M., Demény, A., Fórizs, I., Hegyi, I., Horváth-Kostka, Z.S.R., Móricz, F., Vallner, Z.S., Pálfy, J., 2020. Mercury anomalies and carbon isotope excursions in the western Tethyan Csővár section support the link between CAMP volcanism and the end-Triassic extinction. Glob. Planet. Change 194, 103291. https://doi.org/10.1016/j.gloplacha.2020.103291.

Kozur, H., 1993. First evidence of Liassic in the vicinity of Csővár (Hungary), and its paleogeographic and paleotectonic significance. Jahrbuch der Geologischen Bundesanstalt 136 (1), 89–98.

Kozur, H., Mock, R., 1991. New Middle Carnian and Rhaetian conodonts from Hungary and the Alps. Stratigraphic importance and tectonic implications for the Buda Mountains and adjacent areas. Jahrbuch der Geologischen Bundesanstalt 134 (2), 271–297.

Kozur, H., Mostler, H., 1990. Saturnaliacae Deflandre and some other stratigraphically important Radiolaria from the Hettangian of Lenggries/Isar (Bavaria/Northern Calcareous Alps). Geologisch-Paläontologische Mitteilungen 17, 179–248.

Kukert, H., Riebesell, U., 1998. Phytoplankton carbon isotope fractionation during a diatom spring bloom in a Norwegian fjord. Mar. Ecol. Prog. Ser. 173, 127–137.

Kutzbach, J.E., 1994. Idealized Pangean climates: sensitivity to orbital change. In: Klein, G.D. (Ed.), Pangea: Paleoclimate, Tectonics, and Sedimentation during Accretion, Zenith, and Breakup of a Supercontinent: Geological Society of America Special Paper 288. Geological Society of America, Boulder, Colorado, pp. 41–55.

Kutzbach, J.E., Gallimore, R.G., 1989. Pangaean climates: megamonsoons of the megacontinent. J. Geophys. Res. Atmos. 94 (D3), 3341–3357. https://doi.org/10.1029/JD094iD03p03341.

Laskar, J., Robutel, P., Joutel, F., Gastineau, M., Correia, A.C.M., Levrard, B., 2004. A long-term numerical solution for the insolation quantities of the Earth. Astron. Astrophys 428 (1), 261–285. https://doi.org/10.1051/0004-6361:20041335.

le Goff, J., Recouvreur, A., Reijmer, J.J.G., Mulder, T., Ducassou, E., Perello, M.-C., Hanquiez, V., Gillet, H., Cavailhes, T., Fabregas, N., 2020. Linking carbonate sediment transfer to seafloor morphology: insights from Exuma Valley, the Bahamas. Sedimentology 68 (2), 609–638. https://doi.org/10.1111/sed.12794.

Li, M., Huang, C., Hinnov, L.A., Ogg, J.G., Chen, Z.-Q., Zhang, Y., 2016. Obliquity-forced climate during the Early Triassic hothouse in China. Geology 44 (8), 623–626. https://doi.org/10.1130/G37970.1.

Li, M., Hinnov, L.A., Huang, C., Ogg, J.G., 2018. Sedimentary noise and sea levels linked to land–ocean water exchange and obliquity forcing. Nat. Commun. 9 (1), 1–12. https://doi.org/10.1038/s41467-018-03454-y.

Li, M., Kump, L.R., Hinnov, L.A., Mann, M.E., 2018. Tracking variable sedimentation rates and astronomical forcing in Phanerozoic paleoclimate proxy series with evolutionary correlation coefficients and hypothesis testing. Earth Planet. Sci. Lett. 501, 165–179. https://doi.org/10.1016/j.epsl.2018.08.041.

Li, M., Hinnov, L.A., Kump, L.R., 2019. Acycle: Time-series analysis software for paleoclimate research and education. Comput. Geosci. 127, 12–22. https://doi.org/10.1016/j.cageo.2019.02.011.

Li, M., Huang, C., Ogg, J., Zhang, Y., Hinnov, L., Wu, H., Chen, Z.-Q., Zou, Z., 2019. Paleoclimate proxies for cyclostratigraphy: comparative analysis using a Lower Triassic marine section in South China. Earth Sci. Rev. 189, 125–146. https://doi.org/10.1016/j.earscirev.2019.01.011.

Mann, M.E., Lees, J.M., 1996. Robust estimation of background noise and signal detection in climatic time series. Clim. Chang. 33 (3), 409–445. https://doi.org/10.1007/BF00142586.

Martínez-Braceras, N., Payros, A., Miniati, F., Arostegi, J., Franceschetti, G., Reijmer, J., 2017. Contrasting environmental effects of astronomically driven climate change on three Eocene hemipelagic successions from the Basque-Cantabrian Basin. Sedimentology 64 (4), 960–986. https://doi.org/10.1111/sed.12334.

Marzoli, A., Renne, P.R., Piccirillo, E.M., Ernesto, M., Bellieni, G., de Min, A., 1999. Extensive 200-million-year-old continental flood basalts of the Central Atlantic Magmatic Province. Science 284 (5414), 616–618. https://doi.org/10.1126/science.284.5414.616.

Maurer, F., Hinnov, L., Schlager, W., 2004. Statistical time-series analysis and sedimentological tuning of bedding rhythms in a Triassic basinal succession (Southern Alps, Italy). In: D'Argenio, B., Weissert, H., Ferreri, V., Silva, I. Premoli (Eds.), Cyclostratigraphy: Approaches and Case Histories: SEPM Special Publication, 81, pp. 83–99. https://doi.org/10.2110/pec.04.81.0083.

McElwain, J.C., Beerling, D.J., Woodward, F.I., 1999. Fossil plants and global warming at the Triassic-Jurassic Boundary. Science 285 (5432), 1386–1390. https://doi.org/10.1126/science.285.5432.1386.

Mutti, M., Weissert, H., 1995. Triassic monsoonal climate and its signature in Ladinian-Carnian carbonate platforms (Southern Alps, Italy). J. Sediment. Res. B65 (3), 357–367. https://doi.org/10.1306/D4268252-2B26-11D7-8648000102C1865D.

Nützel, A., Joachimski, M., López Correa, M., 2010. Seasonal climatic fluctuations in the Late Triassic tropics—high-resolution oxygen isotope records from aragonitic bivalve shells (Cassian Formation, Northern Italy). Palaeogeogr. Palaeoclimatol. Palaeoecol. 285, 194–204. https://doi.org/10.1016/j.palaeo.2009.11.011.

Olsen, P.E., Kent, D.V., 1996. Milankovitch climate forcing in the tropics of Pangaea during the late Triassic. Palaeogeogr. Palaeoclimatol. Palaeoecol. 122 (1–4), 1–26. https://doi.org/10.1016/0031-0182(95)00171-9.

Pálfy, J., Demény, A., Haas, J., Carter, E.S., Görög, Á., Halász, D., Oravecz-Scheffer, A., Hetényi, M., Márton, E., Orchard, M.J., Ozsvárt, P., Vető, I., Zajzon, N., 2007. Triassic-Jurassic boundary events inferred from integrated stratigraphy of the Csővár section, Hungary. Palaeogeogr. Palaeoclimatol. Palaeoecol. 244 (1-4), 11–33. https://doi.org/10.1016/j.palaeo.2006.06.021.

Pálfy, J., Demény, A., Haas, J., Hetényi, M., Orchard, M., Vető, I., 2001. Carbon isotope anomaly and other geochemical changes at the Triassic-Jurassic boundary from a marine section in Hungary. Geology 29 (11), 1047–1050. https://doi.org/10.1130/0091-7613(2001)029<1047. CIAAOG >2.0.CO;2.

Pálfy, J., Dosztály, L., 2000. A new marine Triassic-Jurassic boundary section in Hungary. In: Hall, R.L., Smith, P.L. (Eds.), Advances in Jurassic Research 2000. Trans Tech, Zürich, pp. 173–179.

Pálfy, J., Haas, J., 2012. Csővári Mészkő Formáció. In: Főzy, I. (Ed.), Magyarország litosztratigráfiai alapegységei. Jura. Magyarhoni Földtani Társulat, Budapest, pp. 34–36.

Pálfy, J., Kocsis, T.Á., 2014. Volcanism of the Central Atlantic Magmatic Province as the trigger of environmental and biotic changes around the Triassic-Jurassic boundary. In: Keller, G., Kerr, A.C. (Eds.), Volcanism, Impacts and Mass Extinctions: Causes and Effects: Geological Society of America Special Paper, 505, pp. 245–261. https://doi.org/10.1130/2014.2505(12).

Pálfy, J., Mortensen, J.K., Carter, E.S., Smith, P.L., Friedman, R.M., Tipper, H.W., 2000. Timing the end-Triassic mass extinction: first on land, then in the sea? Geology 28 (1), 39–42. https://doi.org/10.1130/0091-7613(2000)28<39. TTEMEF >2.0.CO;2.

Parrish, J.T., 1993. Climate of the Supercontinent Pangea. J. Geol. 101, 215–233. https://doi.org/10.1086/648217.

Peters, S., Husson, J., 2015. Phanerozoic growth of the epicontinental sedimentary reservoir: implications for long-term sea level change. In: 2015 AGU Fall Meeting, San Francisco, CA.

Quye-Sawyer, J., Vandeginste, V., Kimberley, J.J., 2015. Application of handheld energy-dispersive X-ray fluorescence spectrometry to carbonate studies: opportunities and challenges. J. Anal. At. Spectrom. 30, 1490. https://doi.org/10.1039/C5JA00114E.

Reijmer, J.J.G., Sprenger, A., Ten Kate, W.G.H.Z., Schlager, W., Krystyn, L., 1994. Periodicites in the composition of Late Triassic calciturbidites (Eastern Alps, Austria). In: De Boer, P.L., Smith, D.G. (Eds.), Orbital Forcing and Cyclic Sequences: IAS Special Publication 19, pp. 323–343.

Ruhl, M., Deenen, M.H.L., Abels, H.A., Bonis, N.R., Krijgsman, W., Kürschner, W.M., 2010. Astronomical constraints on the duration of the early Jurassic Hettangian stage and recovery rates following the end-Triassic mass extinction (St Audrie's Bay/East Quantoxhead, UK). —. Earth Planet. Sci. Lett. 295 (1-2), 262–276. https://doi.org/10.1016/j.epsl.2010.04.008.

Ruhl, M., Hesselbo, S.P., Al-Suwaidi, A., Jenkyns, H.C., Damborenea, S.E., Manceñido, M.O., Storm, M., Mather, T.A., Riccardi, A.C., 2020. On the onset of Central Atlantic Magmatic Province (CAMP) volcanism and environmental and carbon-cycle change at the Triassic-Jurassic transition (Neuquén Basin, Argentina). Earth Sci. Rev. 208, 103229 https://doi.org/10.1016/j.earscirev.2020.103229.

Ruhl, M., Hesselbo, S.P., Hinnov, L., Jenkyns, H.C., Xu, W., Riding, J.B., Storm, M., Minisini, D., Ullmann, C.V., Leng, M.J., 2016. Astronomical constraints on the duration of the Early Jurassic Pliensbachian Stage and global climatic fluctuations. Earth Planet. Sci. Lett. 455, 149–165. https://doi.org/10.1016/j.epsl.2016.08.038.

Saker-Clark, M., Kemp, D.B., Coe, A.L., 2019. Portable X-Ray fluorescence spectroscopy as a tool for cyclostratigraphy. Geochem.Geophys. Geosyst. 20, 2531–2541. https://doi.org/10.1029/2018GC007582.

Schaltegger, U., Guex, J., Bartolini, A., Schoene, B., Ovtcharova, M., 2008. Precise U-Pb age constraints for end-Triassic mass extinction, its correlation to volcanism and Hettangian post-extinction recovery. Earth Planet. Sci. Lett. 267 (1-2), 266–275. https://doi.org/10.1016/j.epsl.2007.11.031.

Schlager, W., 1992. In: Sedimentology and Sequence Stratigraphy of Reefs and Carbonate Platforms. AAPG, Tulsa, Oklahoma, p. 71.

Schulz, M., Schäfer-Neth, C., 1998. Translating Milankovitch climate forcing into eustatic fluctuations via thermal deep water expansion: a conceptual link. —. Terra Nova 9, 228–231. https://doi.org/10.1111/j.1365-3121.1997.tb00018.x.

Sepkoski, J.J., 1996. Patterns of Phanerozoic Extinction: a Perspective from Global Data Base. In: Walliser, O.H. (Ed.), Global Events and Event Stratigraphy in the Phanerozoic: Results of the International Interdisciplinary Cooperation in the IGCP-Project 216 "Global Biological Events in Earth History". Springer Berlin Heidelberg, Berlin, Heidelberg, pp. 35–51. https://doi.org/10.1007/978-3-642-79634-0_4.

Sha, J., Olsen, P.E., Pan, Y., Xu, D., Wang, Y., Zhang, X., Yao, X., Vajda, V., 2015. Triassic–Jurassic climate in continental high-latitude Asia was dominated by obliquity-paced variations (Junggar Basin, Ürümqi, China). Proc. Nat. Acad. Sci. 112/12, 3624–3629. https://doi.org/10.1073/pnas.1501137112.

Shankar, D., Shetye, S.R., 1999. Are interdecadal sea level changes along the Indian coast influenced by variability of monsoon rainfall? J. Geophys. Res. 104/C11 https://doi.org/10.1029/1999JC900218, 26 031–26 042.

Sinnesael, M., De Vleeschouwer, D., Coccioni, R., Claeys, P., Frontalini, F., Jovane, L., Savian, J.F., Montanari, A., 2016. High-resolution multiproxy cyclostratigraphic analysis of environmental and climatic events across the Cretaceous-Paleogene boundary in the classic pelagic succession of Gubbio (Italy. In: Menichetti, M., Coccioni, R., Montanari, A. (Eds.), The Stratigraphic Record of Gubbio: Integrated Stratigraphy of the Late Cretaceous–Paleogene Umbria-Marche Pelagic Basin: Geological Society of America Special Paper 524, pp. 115–137.

Sinnesael, M., de Vleeschouwer, D., Zeeden, C., Batenburg, S.J., da Silva, A.-C., Dewinter, N.J., Dinarčs-Turell, J., Drury, A.J., Gambacorta, G., Hilgen, F.J., Hinnov, L.A., Hudson, A.J.L., Kemp, D.B., Lantink, M.L., Laurin, J., Li, M., Liebrand, D., Ma, C., Meyers, S.R., Monkenbusch, J., Montanari, A., Nohl, T., Pälike, H., Pas, D., Ruhl, M., Thibault, N., Vahlenkamp, M., Valero, L., Wouters, S., Wu, H., Claeys, P., 2019. The Cyclostratigraphy Intercomparison Project (CIP): consistency, merits and pitfalls. Earth Sci. Rev. 199, 102965 https://doi.org/10.1016/j.earscirev.2019.102965.

Sinnesael, M., De Winter, N.J., Snoeck, C., Montanari, A., Claeys, P., 2018. An integrated pelagic carbonate multi-proxy study using portable X-ray fluorescence (pXRF): Maastrichtian strata from the Bottaccione Gorge, Gubbio, Italy. Cretaceous Res. 91, 20–32. https://doi.org/10.1016/j.cretres.2018.04.010.

Southam, J.R., Hay, W.W., 1981. Global sedimentary mass balance and sea level changes. —. In: Emiliani, C. (Ed.), The Ocean Lithosphere, the Sea 7. John Wiley and Sons, New York, pp. 1617–1684.

Storm, M.S., Hesselbo, S.P., Jenkyns, H.C., Ruhl, M., Ullmann, C.V., Xu, W., Leng, M.J., Riding, J.B., Gorbanenko, O., 2020. Orbital pacing and secular evolution of the Early Jurassic carbon cycle. —. PNAS 117 (8), 3974–3982. https://doi.org/10.1073/pnas.1912094117.

Strasser, A., Hilgen, F.J., Heckel, P.H., 2007. Cyclostratigraphy concepts, definitions, and applications. Newsl. Stratigr. 42 (2), 75–114. https://doi.org/10.1127/0078-0421/2006/0042-0075.

Thomson, D.J., 1982. Spectrum estimation and harmonic analysis. In: Proceedings of the IEEE 70/9, pp. 1055–1096. https://doi.org/10.1109/PROC.1982.12433.

Torrence, C., Compo, G.P., 1998. A practical guide to wavelet analysis. Bull. Am. Meteorol. Soc. 79, 61–78. https://doi.org/10.1175/1520-0477(1998)079<0061. APGTWA >2.0.CO;2.

Wagreich, M., Lein, R., Sames, B., 2014. Eustasy, its controlling factors, and the limno-eustatic hypothesis – concepts inspired by Eduard Suess. Austr. J. Earth Sci. 107 (1), 115–131.

Ward, P.D., Haggart, J.W., Carter, E.S., Wilbur, D., Tipper, H.W., Evans, T., 2001. Sudden productivity collapse associated with the Triassic-Jurassic boundary mass extinction. Science 292 (11), 1148–1151. https://doi.org/10.1126/science.1058574.

Weedon, G., 2003. Time-Series Analysis and Cyclostratigraphy: Examining Stratigraphic Records of Environmental Cycles. — Cambridge University Press, Cambridge. https://doi.org/10.1017/CBO9780511535482.

Weedon, G.P., Jenkyns, H.C., Coe, A.L., Hesselbo, S.P., 1999. Astronomical calibration of the Jurassic time-scale from cyclostratigraphy in British mudrock formations. Philos. Trans. Roy. Soc. Ser.A 357, 1787–1813. https://doi.org/10.1098/rsta.1999.0401.

Weedon, G.P., Page, K.N., Jenkyns, H.C., 2019. Cyclostratigraphy, stratigraphic gaps and the duration of the Hettangian Stage (Jurassic): insights from the Blue Lias Formation of southern Britain. Geol. Mag. 156 (9), 1469–1509. https://doi.org/10.1017/S0016756818000808.

Wendler, J.E., Wendler, I., Vogt, C., Kuss, J., 2016. Link between cyclic eustatic sea-level change and continental weathering: evidence for aquifer-eustasy in the cretaceous. Palaeogeogr. Palaeoclimatol. Palaeoecol. 441 (3), 430–437. https://doi.org/10.1016/j.palaeo.2015.08.014.

Westphal, H., Hilgen, F., Munnecke, A., 2010. An assessment of the suitability of individual rhythmic carbonate successions for astrochronological application. Earth Sci. Rev. 99 (1–2), 19–30. https://doi.org/10.1016/j.earscirev.2010.02.001.

Whiteside, J.H., Olsen, P.E., Eglinton, T., Brookfield, M.E., Sambrotto, R.N., 2010. Compound-specific carbon isotopes from Earth's largest flood basalt eruptions directly linked to the end-Triassic mass extinction. PNAS 107 (15), 6721–6725. https://doi.org/10.1073/pnas.1001706107.

Xu, W., Ruhl, M., Hesselbo, S.P., Riding, J.B., Jenkyns, H.C., 2017. Orbital pacing of the Early Jurassic carbon cycle, black-shale formation and seabed methane seepage. Sedimentology 64 (1), 127–149. https://doi.org/10.1111/sed.12329.

Yager, J.A., West, A.J., Corsetti, F.A., Berelson, W.M., Rollins, N.E., Rosas, S., Bottjer, D. J., 2017. Duration of and decoupling between carbon isotope excursions during the end-Triassic mass extinction and Central Atlantic Magmatic Province emplacement. Earth Planet. Sci. Lett. 473, 227–236. https://doi.org/10.1016/j.epsl.2017.05.031.

Yamasaki, T., 2018. Contamination from mortars and mills during laboratory crushing and pulverizing. Bull. Geol. Survey Japan 69 (3), 201–210. https://doi.org/10.9795/bullgsj.69.201.

Yao, X., Hinnov, L.A., 2019. Advances in characterizing the cyclostratigraphy of binary chert-mudstone lithologic successions, Permian (Roadian-lower Capitanian), Chaohu, Lower Yangtze, South China. Palaeogeogr. Palaeoclimatol. Palaeoecol. 528, 258–271. https://doi.org/10.1016/j.palaeo.2019.05.004.